AD-A085 023　NORTHROP CORP　ANAHEIM CA　ELECTRO-MECHANICAL DIV　F/G 17/5
AUTOMATIC TARGET CUER.(U)
FEB 80　B DEAL, C M LO, R TAYLOR, V NORWOOD　DAAK70-79-C-0066
UNCLASSIFIED　NORT-80Y007　NL

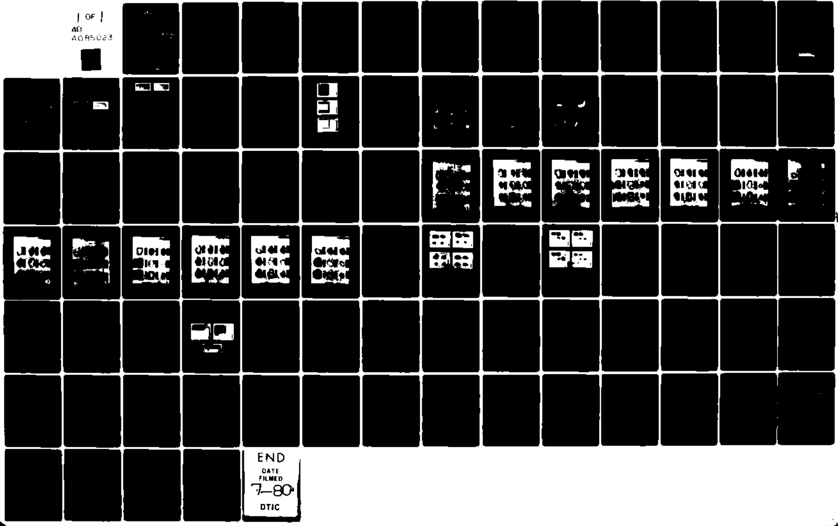

END
DATE
FILMED
7-80
DTIC

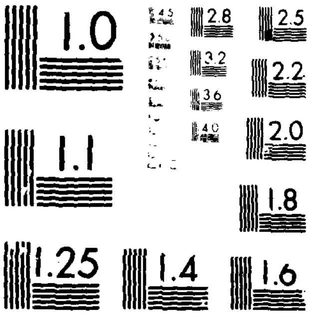
1.0
2.8
2.5
3.2
2.2
3.6
4.0
2.0
1.1
1.8
1.25
1.4
1.6

80Y007

2

AUTOMATIC TARGET CUER
SECOND QUARTER REPORT

Prepared by

B. Deal
C. M. Lo
R. Taylor
V. Norwood
T. Daggett
T. Noda
J. Powers
G. Guzman
H. Greenberger
G. Parker

NORTHROP CORPORATION
Electro-Mechanical Division
500 East Orangethorpe Avenue
Anaheim, California 92801

1 February 1980

QUARTER REPORT
FOR PERIOD
1 September 1979 — 31 December 1979

APPROVED FOR PUBLIC RELEASE
Distribution Unlimited

NIGHT VISION AND ELECTRO-OPTICS LABORATORY
FORT BELVOIR, VIRGINIA 22060

UNCLASSIFIED

SECURITY CLASSIFICATION OF THIS PAGE (When Data Entered)

REPORT DOCUMENTATION PAGE

READ INSTRUCTIONS BEFORE COMPLETING FORM

1. REPORT NUMBER 80Y007	2. GOVT ACCESSION NO. AD-A085023	3. RECIPIENT'S CATALOG NUMBER
4. TITLE (and Subtitle) ⑥ AUTOMATIC TARGET CUER. SECOND QUARTER REPORT		5. TYPE OF REPORT & PERIOD COVERED ⑨ QUARTERLY PROGRESS REPORT, no. 2, 1 SEPT — 31 DEC [redacted] 79 6. PERFORMING ORG. REPORT NUMBER 14 NORT — 80Y007
7. AUTHOR(s) ⑩ B. Deal, C.M. Lo, R. Taylor, V. Norwood, T. Daggett, T. Noda, J. Powers, G. Guzman, H. Greenberger, G. Parker	⑮	8. CONTRACT OR GRANT NUMBER(s) DAAK70-79-C-0066
9. PERFORMING ORGANIZATION NAME AND ADDRESS Northrop Electro-Mechanical Division 500 East Orangethorpe Avenue Anaheim, California 92801		10. PROGRAM ELEMENT, PROJECT, TASK AREA & WORK UNIT NUMBERS ⑫ 85
11. CONTROLLING OFFICE NAME AND ADDRESS Night Vision and Electro-Optics Laboratory Fort Belvoir, VA 22060	⑪	12. REPORT DATE 1 Feb [redacted] 80 13. NUMBER OF PAGES 84
14. MONITORING AGENCY NAME & ADDRESS (if different from Controlling Office)		15. SECURITY CLASS. (of this report) UNCLASSIFIED 15a. DECLASSIFICATION/DOWNGRADING SCHEDULE

16. DISTRIBUTION STATEMENT (of this Report)

Approved for public release distribution unlimited.

17. DISTRIBUTION STATEMENT (of the abstract entered in Block 20, if different from Report)

18. SUPPLEMENTARY NOTES

19. KEY WORDS (Continue on reverse side if necessary and identify by block number)

Infrared
FLIR
Target Cuer
Target Recognition
Image Enhancement
Image Segmentation

This report

20. ABSTRACT (Continue on reverse side if necessary and identify by block number)

This is the second quarterly progress report for the ATC program. It covers system organization and specific algorithm development, leading to the construction of a real-time target cueing system. for the ATC program

DD FORM 1 JAN 73 1473 EDITION OF 1 NOV 65 IS OBSOLETE

UNCLASSIFIED 388834

SECURITY CLASSIFICATION OF THIS PAGE (When Data Entered)

80Y007

CONTENTS

CONTENTS (Continued)

Illustrations

Illustrations (Continued)

Tables

SECTION 1
INTRODUCTION

This is the second quarterly progress report for the Automatic Target Cuer (ATC) Program, Contract No. DAAK70-79-C-0066. The ATC Program is a 30-month effort which will culminate in the delivery of two developmental ATC systems to the Night Vision and Electro-Optics Laboratory (NV&EOL). The first system will be in an engineering, breadboard-type configuration, while the second system will be an airworthy unit and integrated with the Light Observation Helicopter Target Acquisition/Designation System (LOHTADS). Flight tests will be conducted with the second unit.

The LOHTADS operator currently would benefit from automated assistance for target acquisition and sensor operation. The goal of the ATC system is to aid in the performance of his tasks by providing target cues and by performing automatic contrast enhancement and control for the displayed image.

The ATC program is divided into three phases. Phase I (6 months) is the system analysis and design effort that primarily includes algorithm development and tradeoff studies. Also included in Phase I is the design and construction of the ATC interfaces and memories. Phase II (13 months) is a modeling and construction phase. The hardware and software specified and designed during Phase I will be constructed during this effort. The specific hardware functions of the ATC will also be modeled, in software, to facilitate system analysis and test. Phase II culminates with the completion of the Model 1 ATC system. During the third phase (11 months), which is primarily a construction and test phase, the Model 2 ATC system will be built. Construction of the Model 2 ATC will basically be a repackaging of the Model 1 system in an airworthy configuration. Tests will be conducted on both the Model 1 and Model 2 systems during Phase III.

This report will describe the progress in the design of the processing algorithms and hardware currently undergoing development as part of Phase I. Plans for the technical effort of the third quarter are also presented.

SECTION 2
ENHANCEMENT ALGORITHM DEFINITION

In the first quarter report, seven different enhancement algorithms were described and evaluated. Each of these algorithms involved a different level of computational complexity and yielded different psychovisual results. All seven competed with each other in terms of the psychovisual result of the final enhanced image.

Through subjective criteria the number of candidate algorithms was reduced to three. A poll was taken of observers to determine the ranking of the algorithms in terms of being psychovisually pleasing. Through this poll it was shown that variable threshold zonal filtering, the prototype automatic target screener enhancement method, and unsharp masking were the enhancement algorithms that gave the most satisfying results.

During this quarter the complexities of the three algorithms were compared. An algorithm that demanded a high degree of computation but yielded an image no more visually pleasing than another algorithm that involved considerably less computation was rejected as a candidate. Of the three final candidates, variable threshold zonal filtering has been selected as the enhancement algorithm to be used in the Automatic Target Cuer (ATC) because analysis showed that it yielded the highest quality images, but required no greater amount of computation than the two other candidates.

2.1 BLOCK DIAGRAM DISCUSSION

Figure 2-1 is a block diagram of the hardware implementation of the variable threshold zonal filtering enhancement algorithm. Each horizontal line of input from the Forward-Looking Infrared (FLIR) consists of 1280 pels, with each pel consisting of 8 bits. A 2-pel integrator reduces the number of independent pels to 640 pels per line. As each 640-pel line flows in, it is sent in two directions. It is sent into a time delay circuit for future use, since all the original values must be used in upcoming calculations. It is also sent into a 4-pel integrator to obtain a sample point with spatial domain that is equal distance in both horizontal and vertical directions. The 640-pel line has now been reduced to a 160-independent pel line.

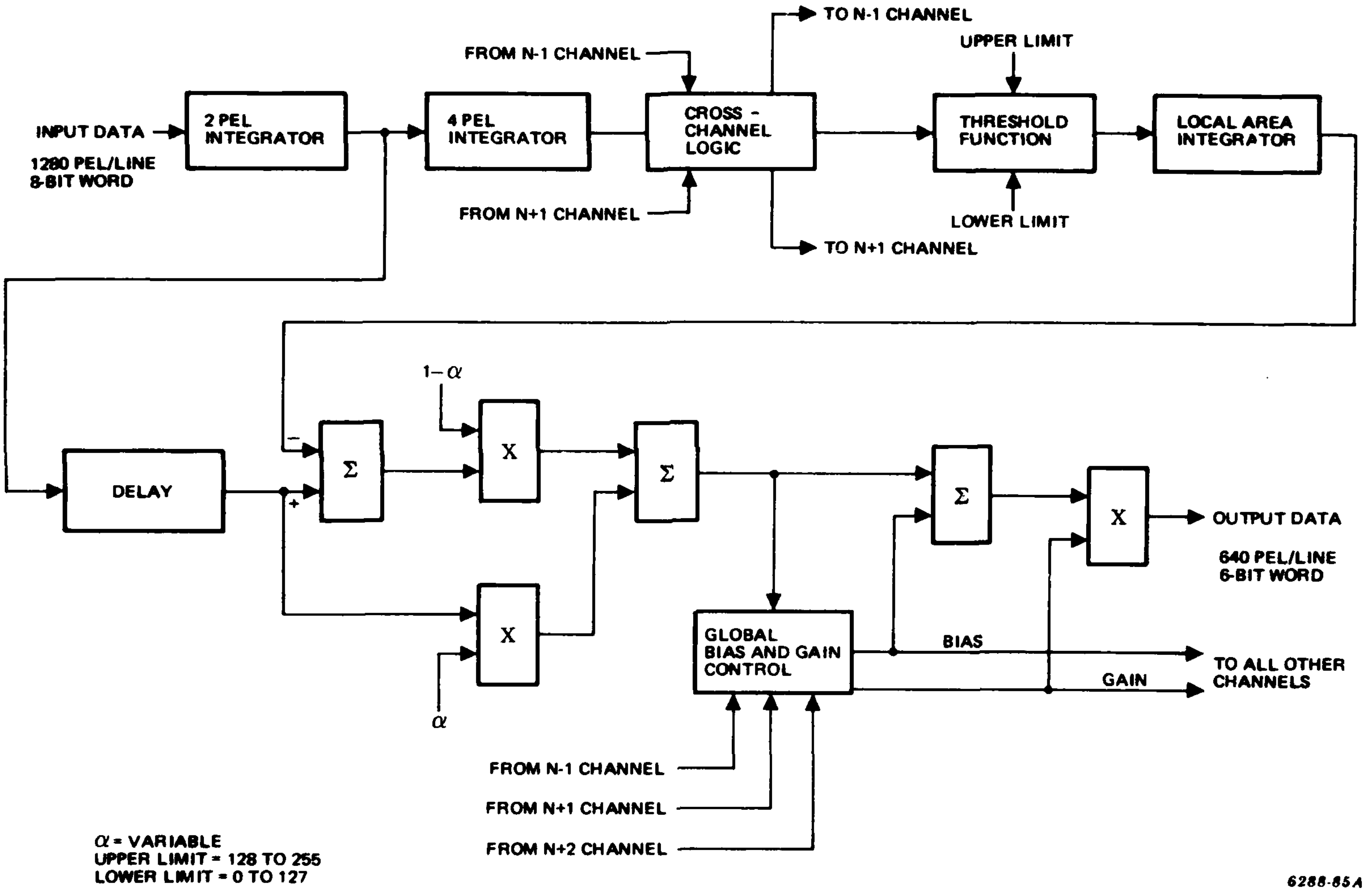

Figure 2-1. Automatic Gain and Brightness (Variable Threshold and Zonal Filter) — Block Diagram

Using this new line and similar lines from the adjacent multiplex channels (N-1 and N+1), the 9 independent pel values used in the enhancement algorithm are retrieved. They are passed through a threshold function and then into a local area integrator to determine the average. The upper and lower limit inputs to the threshold function are preset values. The average and the original pel value, obtained from the delay circuit, are then passed to a summing circuit. The original pel value is added and the average subtracted in this circuit. The value from this summation is then passed to a multiplication circuit where it is multiplied by $(1-\alpha)$. The original pel value is also passed to a multiplication circuit where it is multiplied by α. The value of α utilized is input from the ATC front panel. The results of these two multiplication circuits are then sent to another circuit to be summed. Global bias and gain control from this channel and the other channels provide bias and gain for the output from this last summation. The global control ensures that the output image data spans the entire gray level range. Output line from this process consists of 640 6-bit words.

2.2 ALGORITHM OPTIONS

The variable threshold zonal filtering enhancement technique initially posed several possible options concerning the final form of the algorithm to be implemented in hardware. These options included the form of threshold to be employed, the gradation to be used in the threshold values and 6-bit precision versus 8-bit precision in the final enhanced image. These options were implemented in a computer simulation of the planned hardware design. Discussions of these options and pictorial examples showing their results are contained in the following sections. The image used for evaluation was taken from the Night Vision and Electro-Optics Laboratory (NV&EOL) Fort Polk 1 data set and is given in Figure 2-2.

6288-86

Figure 2-2. Original Image Used for Evaluation

2.2.1 Gradation of Threshold Values

Part of the enhancement algorithm thresholds the original image data thereby reducing the range of gray values used to calculate the local average. This threshold occurs at both the upper and lower ends of the gray-scale range. To reduce the hardware complexity of the ATC final system, it is desirable to have possible threshold values cover the range 0 to 225 but gradated in units of 16 gray levels. To determine whether this gradation for threshold values was too coarse, the original image was enhanced using this gradated range of thresholds. Visual interpretation of the enhanced images showed that there was no appreciable difference between two successive threshold values on the same original image. Figure 2-3 shows examples of this form of threshold where the increment or decrement in the threshold level was 16.

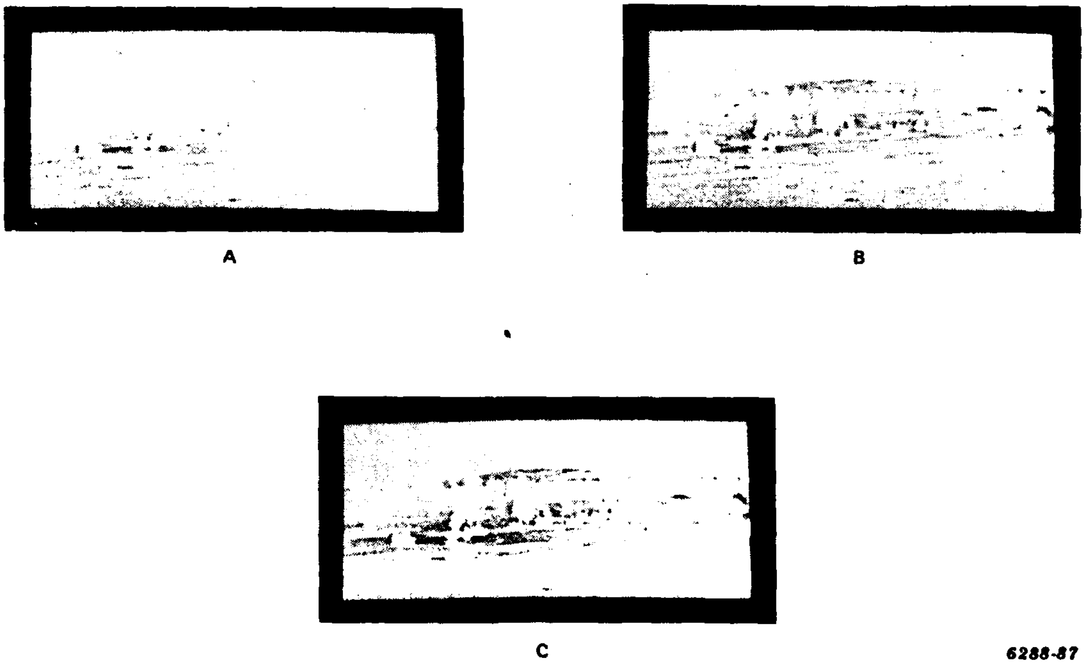

6288-87

Figure 2-3. Effects of Consecutive Thresholds

2.2.2 Hard Threshold versus Soft Threshold

Hard threshold is defined as that form of threshold where values outside any particular threshold bound will be set to zero. Soft threshold is defined as that form of threshold where values beyond any particular threshold bound level will be set to that threshold level. Figure 2-4 shows examples of soft threshold and hard threshold respectively. All other parameters in these enhanced images are identical. Soft threshold gives a more pleasing image and is clearly the brighter of the two. Hard threshold tends to give a more abrupt change in tonal gradation of the image. Therefore, soft threshold was selected for use in the ATC.

SOFT THRESHOLD HARD THRESHOLD 6288-88

Figure 2-4. Effects of Threshold Values

2.2.3 6-Bit Versus 8-Bit Precision

To ease hardware complexity in the scan converter, it is highly desirable to output the enhanced image in 6-bit precision versus the 8-bit precision of the original image. The 8 bits of the original image gave 256 possible gray levels where the 6 bits of the enhanced image yielded 64 possible gray levels. Possible image degradation as a result of the loss of 2 bits in precision of the output image was investigated by comparing enhanced images using 6-bit with those using 8-bit precision in the displayed image. When using the same original image for enhancement, no noticeable difference was apparent between the 6-bit and the 8-bit precision output. Figure 2-5 shows examples of 6-bit and 8-bit output.

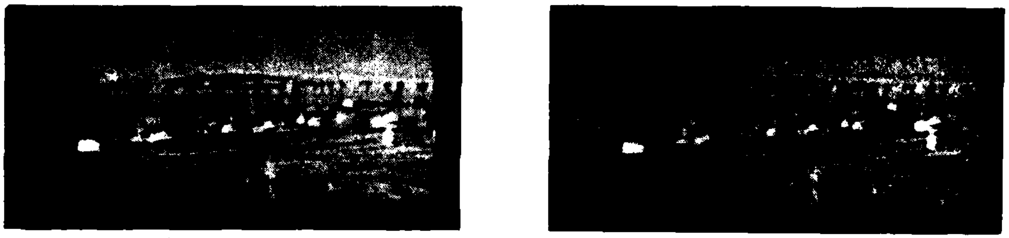

8-BIT OUTPUT

6-BIT OUTPUT

6288-89

Figure 2-5. Precision Effects of Output

2.3 SUMMARY AND STATUS

Variable threshold zonal filtering has been chosen as the algorithm to be used for image enhancement for use in the FLIR image processor. The proposed form of implementation of this enhancement algorithm in hardware brought with it several options. These options concerned the bit precision of the output image and form of threshold. It was shown that no noticeable difference exists between an image with 8-bit precision and the identical image with only 6-bit precision. Soft threshold was chosen since it yielded the more pleasing results. The precision of the threshold levels was set to be four bits or one every 16 gray levels. This is allowable since no significant difference occurs between enhanced images using successive thresholds. Thus, this system optimizes the enhancement algorithm for its implementation into hardware.

The hardware design for enhancement has been completed and the enhancement circuit cards have been wire-wrapped. The enhancement circuitry occupies five 8" x 10" cards in the ATC main frame (one card per multiplex channel with one card as a controller). During the next quarter the enhancement circuits will enter their test and debug phase.

SECTION 3
TARGET DETECTION

The target detector in the Automatic Target Cuer (ATC) system communicates with both the frame store memory and the silhouetter. The detector scans the entire frame store memory searching for targets and informs the silhouetter of candidate target locations. The design goal for the detector is a P_d of .98 with a FAR less than 10 per frame. Two functions are required of the target detector. One is the actual target detection itself, where targets are filtered out of the image, and the other where target window coordinates are generated so the frame store can pass target subframes to the silhouetting algorithm. This section will describe both the target filtering process and the target locating process.

3.1 TARGET FILTERING

Target filtering is performed by a set of filters that look for two basic target primatives — high-contrast corners and high-contrast spots. Corner filtering is achieved by examining the Haar transform coefficients of the square Haar basis functions, and spot filtering is effected by corner-filtering the output of the corner filter. The results of each filtering operation are then weighted and summed across the entire image plane. The summed output then is subjected to a spatial low-pass filter and a threshold value. A block diagram of this process is illustrated in Figure 3-1.

The structure of the detection process is such that a linear classification of target and nontarget regions is performed using the outputs of the target filters as input features. The weights, w_i, and the threshold Θ_T can all be derived using standard training techniques. The low-pass filter used in this case is a 17 x 17 box filter.

The detection output for two values of threshold is shown in Figure 3-2. The output of the target detection function is a binary valued image where the target locations have been turned into blobs representing the target locations. The remainder of the target detector subsystem then must generate the coordinates for a window with the target in the center.

3.2 TARGET LOCATER

The target locater examines the entire image after targets have been detected and outputs appropriately centered window coordinates to the silhouetter.

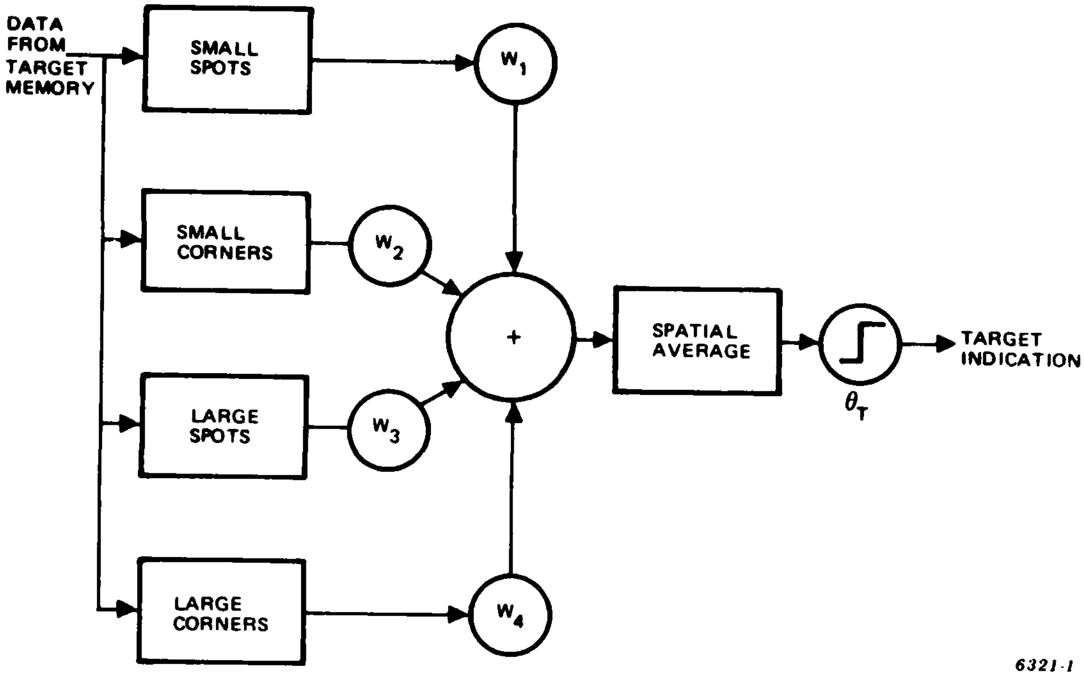

Figure 3-1. Target Detection Block Diagram Using Corners and Spots

Target location may be described functionally as a two-step process. First, an array of rectangular bins is overlaid on the image, and encoded with a number describing the distribution of target blobs within each bin. In the second step, the codes of each bin are compared with those of its neighbors in an effort to find the approximate target blob center for window construction. A block diagram of the target location process is shown in Figure 3-3.

3.2.1 Bin Encoding

A bin structure that overlays the image in the frame store is illustrated in Figure 3-4. The size of the bin is arbitrary but in the current implementation it is taken to be 20 pixels high and 8 pixels wide. This size is convenient for simulation purposes because it is identical to the area subtended by the annotation memory in the laboratory frame store. However, in the actual ATC implementation, bin sizes would differ in terms of pixels due to the nonsquare resolution of the sensor. Also, the hardware is simplified if powers of two increments are used for the bin dimensions.

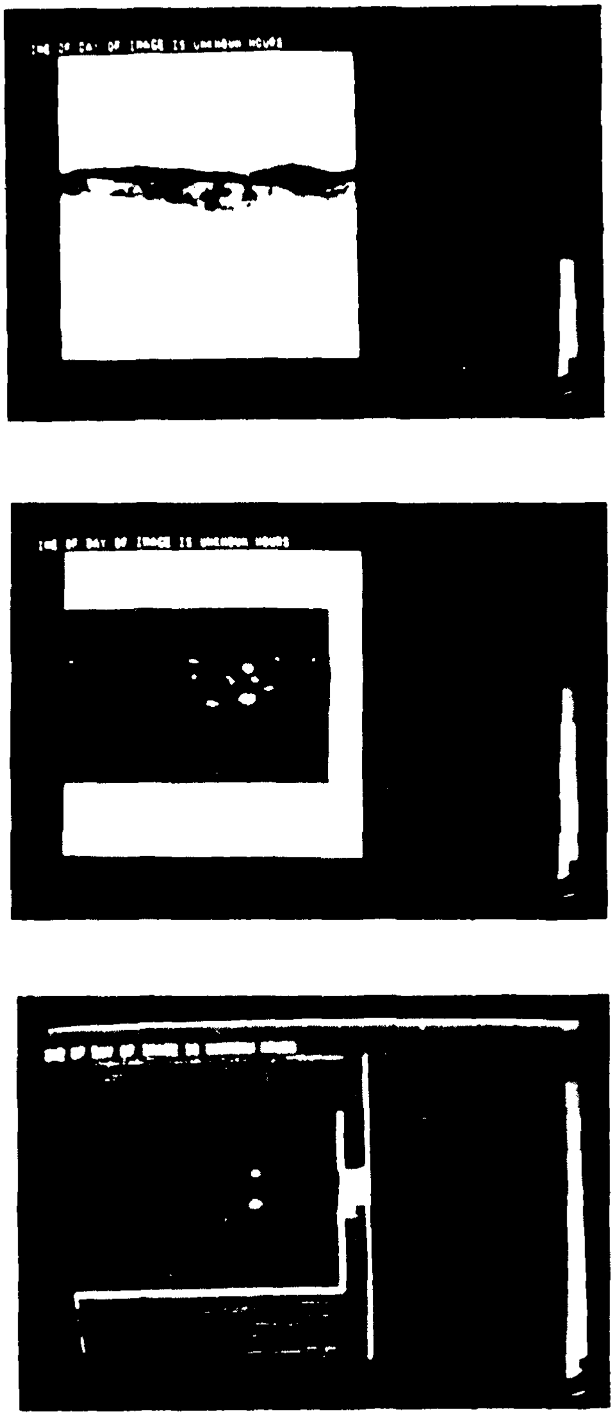

HUNTER-LIGGET
ORIGINAL FRAME

DETECTED TARGETS
$\theta = 20$

DETECTED TARGETS
$\theta = 40$

6288-63(4)

Figure 3-2. Target Detection Example

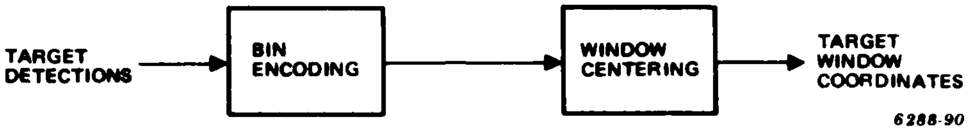

Figure 3-3. Target Locater Block Diagram

Each bin is further subdivided into four equal quadrants. Each quadrant has a specific code. If, in any quadrant, a binary-valued "1" is present as a target indication, that quadrant's code is added arithmetically to the code for the entire bin. An enlargement of a bin and the corresponding codes for each of the quadrants are shown in Figure 3-5. For example, if there is target indication in the upper right-hand corner of the bin and no other target indications in any other quadrant, then the bin would be assigned the numerical value 8. An example of detected target shapes overlaying the quadrants in various patterns is shown in Figure 3-6. The corresponding bin codes for each of the shape

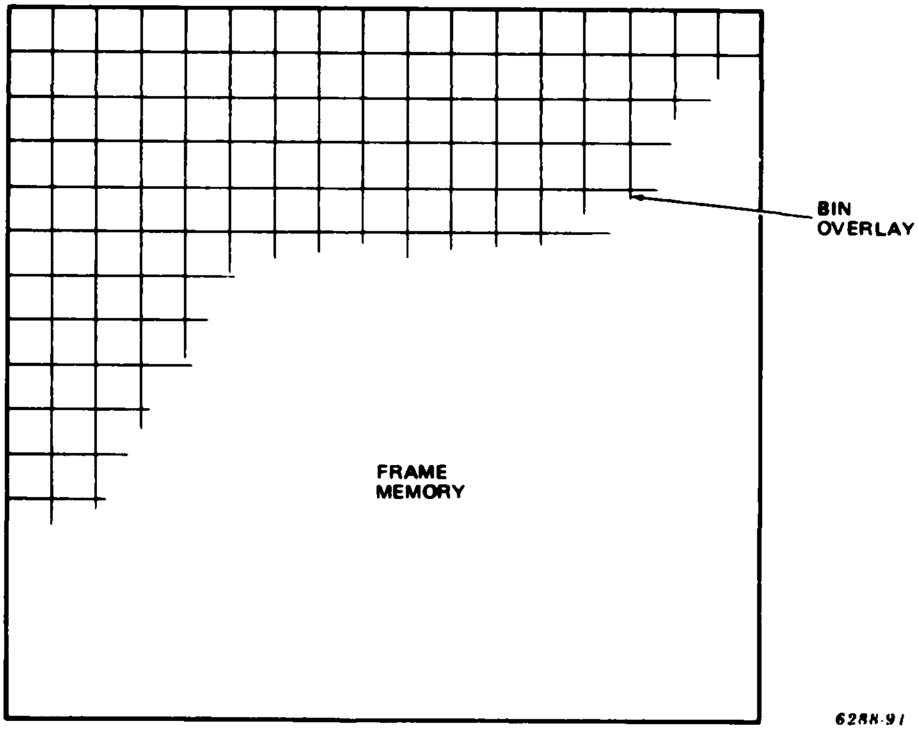

Figure 3-4. Subdivision of Frame Memory

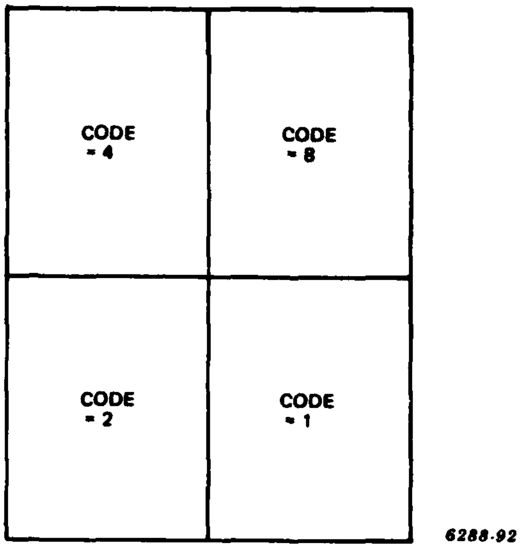

Figure 3-5. Bin Encoding Scheme

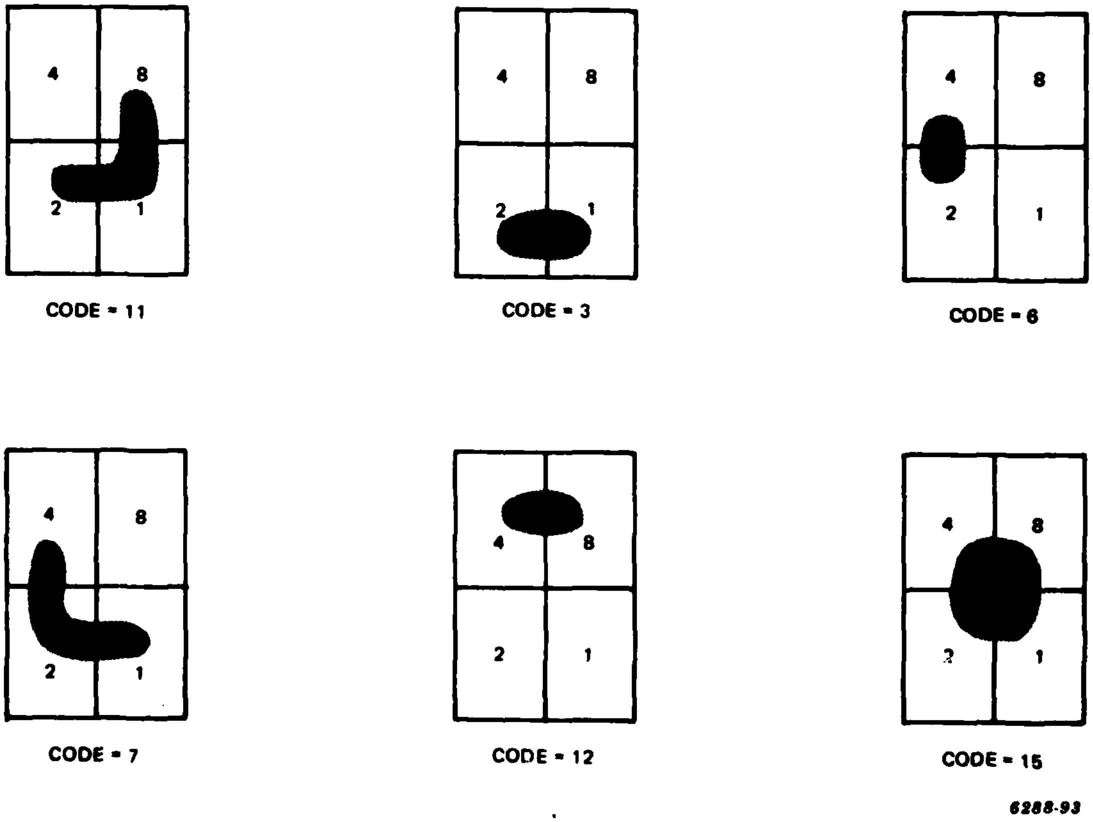

Figure 3-6. Examples of Bin Codes for Targets Overlapping Quadrants

configurations are given below each bin. By coding the bins in this fashion, the distribution of target shape within the bin array may be summarized. This summary is used to find the appropriate centers of target windows. It is also used for determining conditions when the target overlaps the bin boundary or cannot be fully contained within a single bin.

3.2.2 Window Centering

Window centering is performed by examining the codes in the array of bins. The resultant center of the window may be determined by the code within a single bin or by a group of bins. In the single-bin case, the code for that particular bin is isolated (i.e., it is surrounded by codes of zeroes for its neighbors). An example of single-bin centering is shown in Figure 3-7. The target shape subtends three quadrants of the bin — quadrant number 2, quadrant number 1, and quadrant number 8. The resultant code, which is 11, within the bin leads to an offset four pixels to the right and four pixels down. The coordinates of the grid element center are 207 and 119 in this particular case. The offsets that are added for a bin code of 11 are four in the vertical direction and four in the horizontal direction. This arrives at a window center value of 211 in the horizontal direction and 123 in the vertical direction.

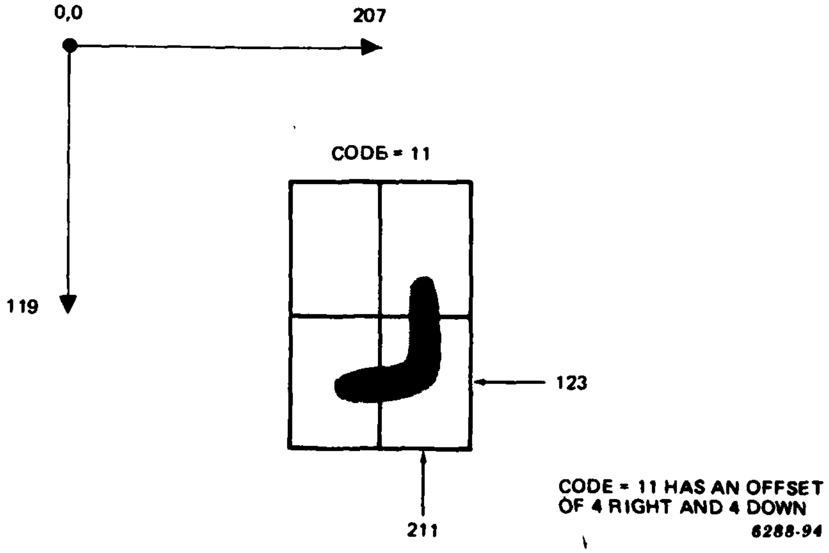

Figure 3-7. Single-Bin Centering

In cases where targets overlap the bin boundaries, further refinements on the center point decisions must be made. In order to determine the overlapped conditions, a table that compares the codes between neighboring bins is utilized. The conditions that form the table for several connected and nonconnected cases are illustrated in Figure 3-8. If the codes of two neighboring bins are 3 and 2, as shown in Figure 3-8, Part A, then a target is assumed to be in the presented location. On the other hand, if the bin codes are 2 and 9, as shown in Figure 3-8, Part C, then the targets are assumed not to be connected.

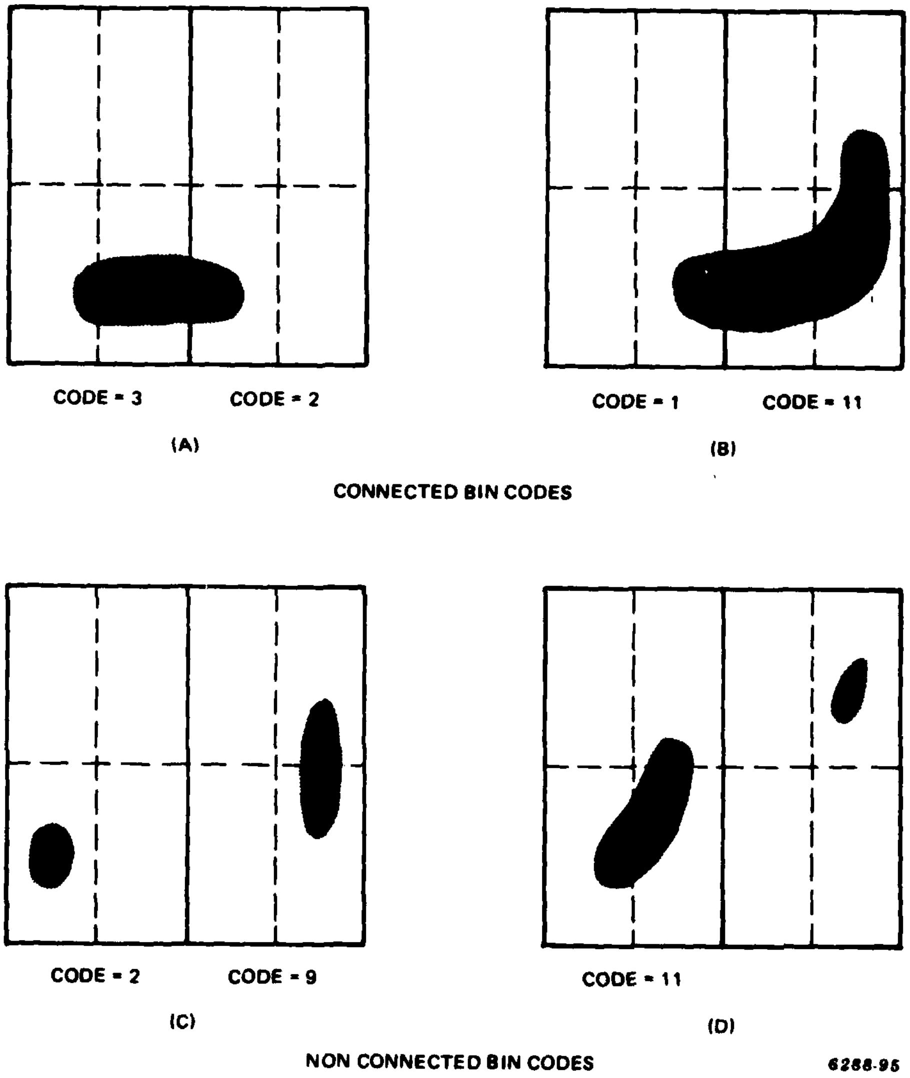

Figure 3-8. Examples of Bin Connections in Horizontal Direction

A truth table of this nature has been constructed for connectivity in both the x and y direction in the image plane. The connectivity tables for both the x and y directions are presented in Table 3-1. Targets are centered according to the following algorithm: (1) The images are scanned in a raster-scanned format until a nonzero bin is reached. (2) That bin's neighbors are then interrogated to see if connectivity exists between that bin and the one immediately to the right and the one immediately below it. (3) If they are connected, the target centers that occur from each bin are averaged into the target center for the connected cluster. (4) Repeat this process in a raster-scanned format until all connected bins within the cluster have been exhausted. (5) Scan to the next nonzero bin.

Table 3-1. Bin Connectivity Tables

X CONTINUITY TABLE

BIN TO THE RIGHT

CURRENT BIN	1	2	3	4	5	6	7	8	9	10	11	12	13	14	15
1	0	1	1	0	0	1	1	0	0	0	0	0	0	0	1
2	0	0	0	0	0	0	0	0	0	0	0	0	0	0	0
3	0	1	1	0	0	1	1	0	0	0	0	0	0	0	1
4	0	0	0	0	0	0	0	0	0	0	0	0	0	0	0
5	0	0	0	0	0	0	0	0	0	0	0	0	0	0	0
6	0	0	0	0	0	0	0	0	0	0	0	0	0	0	0
7	0	1	1	0	0	1	1	0	0	0	0	0	0	0	1
8	0	0	0	1	0	1	1	0	0	0	0	1	1	1	1
9	0	1	1	1	0	1	1	0	0	0	0	1	0	1	1
10	0	0	0	0	0	0	0	0	0	0	0	0	0	0	0
11	0	1	1	1	0	1	1	0	0	0	0	1	0	1	1
12	0	0	0	1	0	1	1	0	0	0	0	1	1	1	1
13	0	1	1	1	0	1	1	0	0	0	0	1	0	1	1
14	0	0	0	1	0	1	1	0	0	0	0	1	1	1	1
15	0	1	1	1	0	1	1	0	0	0	0	1	0	1	1

Y CONTINUITY TABLE

BIN BELOW

CURRENT BIN	1	2	3	4	5	6	7	8	9	10	11	12	13	14	15
1	0	0	0	0	0	0	0	1	1	0	0	1	1	0	1
2	0	0	0	1	0	1	1	0	0	0	0	1	1	1	1
3	0	0	0	1	0	1	0	1	1	0	0	1	1	1	1
4	0	0	0	0	0	0	0	0	0	0	0	0	0	0	0
5	0	0	0	0	0	0	0	0	0	0	0	0	0	0	0
6	0	0	0	1	0	1	1	0	0	0	0	1	1	1	1
7	0	0	0	1	0	1	0	1	1	0	0	1	1	1	1
8	0	0	0	0	0	0	0	0	0	0	0	0	0	0	0
9	0	0	0	0	0	0	0	1	1	0	0	1	1	0	1
10	0	0	0	0	0	0	0	0	0	0	0	0	0	0	0
11	0	0	0	1	0	1	0	1	1	0	0	1	1	1	1
12	0	0	0	0	0	0	0	0	0	0	0	0	0	0	0
13	0	0	0	0	0	0	0	1	1	0	0	1	1	0	1
14	0	0	0	1	0	1	1	0	0	0	0	0	1	1	1
15	0	0	0	1	0	1	0	1	1	0	0	1	1	1	1

SECTION 4
TARGET SILHOUETTING

During the previous quarter, several deficiencies were noted in the target silhouetting system that was described: (1) the method used to select thresholds only looked at the brighter half of the gray scale histogram, (2) the edge detection and thinning algorithms produced noisy and fragmented edges, (3) multiple silhouettes within the subframe were not addressed, and (4) silhouetting algorithms needed to be tested on a larger data base.

The silhouetting system was described in the first Automatic Target Cuer (ATC) quarterly report and is shown in a slightly modified form as Figure 4-1. The one-dimensional histogram has been removed, and the connected component function is shown. Also, after edge thinning, the figure of merit computation is identified as a separate function. This latter change was instituted for ease of system partitioning.

This section will present improved procedures for edge detection, edge thinning, and threshold selection. A test is described, and results are presented.

4.1 EDGE DETECTION

In edge detection we are interested in obtaining the boundary of an object. There are two basic approaches to the image detection: the enhancement/threshold method and the edge fitting method[1]. We adopted the enhancement/threshold method for edge detection, and its system is described in Figure 4-2. In this method, the filtered subimage array F(j,K) is spatially processed by a set of N linear operators or masks W_i to produce a set of gradient functions

$$G_i(j,K) = F(j,K) \circledast W_i(j,K) \tag{1}$$

where $\circledast$ denotes two-dimensional spatial convolution.

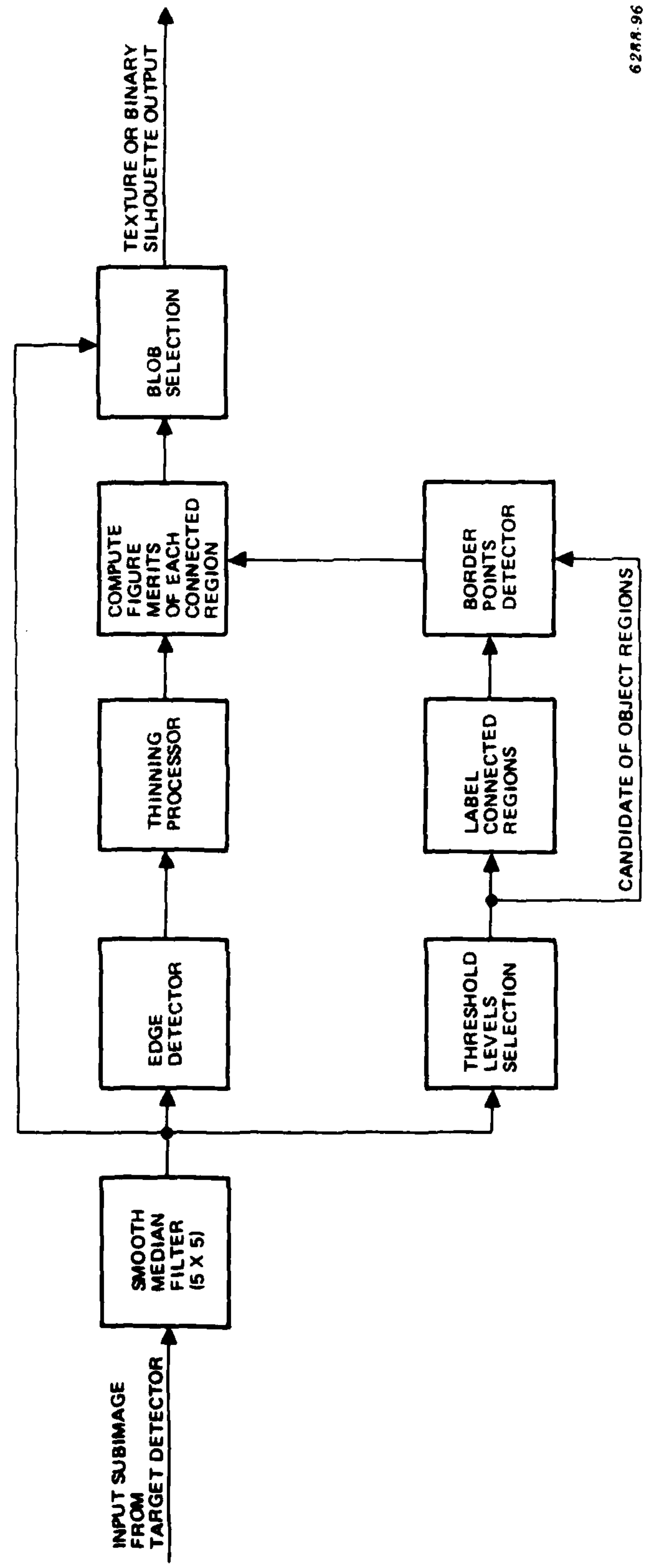

Figure 4-1. Target Silhouetter System

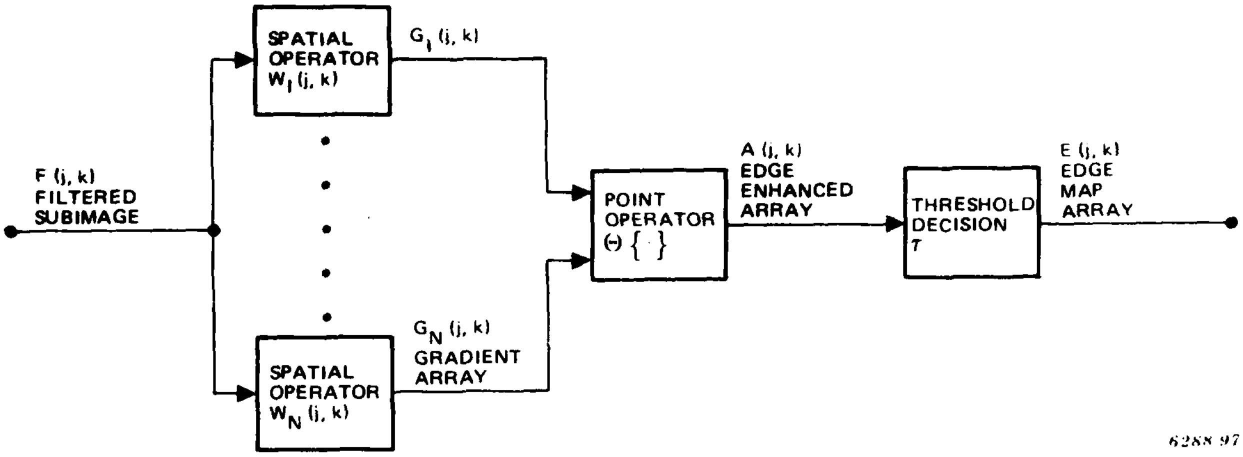

Figure 4-2. Edge Detection System

Next, at each pixel, the gradient functions are combined by an operator $\{\Theta\}$ to create an edge-enhanced array

$$A(j,K) = \Theta\{G_i(j,K)\}. \qquad (2)$$

Typical forms of the point operator $\{\Theta\}$ include the root mean square (rms), magnitude, and maximum. The result of this operation, A(j,K), is thresholded to produce the edge map array E(j,K). This block diagram holds for all edge detection procedures used in the previous quarter effort.

Frei and Chen[2] have presented a set of spatial edge masks that span a 9-dimensional orthogonal vector space. The basis vectors are shown in Figure 4-3. These masks or combinations of these masks represent every possible orientation edge that could occur in the subimage. They also have further partitioned the vector space into subspaces that are sensitive to edges and lines respectively. The vector W_9 is added to complete the space. When all the basis vectors are used, the computation load necessary to obtain the edge may array is greatly increased. As suggested by Frei and Chen[2] and studied by Professor T. S. Huang's group at MIT[3], some of the basis vectors contribute little information to the edge detection. Therefore, only the most significant masks W_1, W_2, W_6, and W_7 were used for the spatial operators of the new edge detection system.

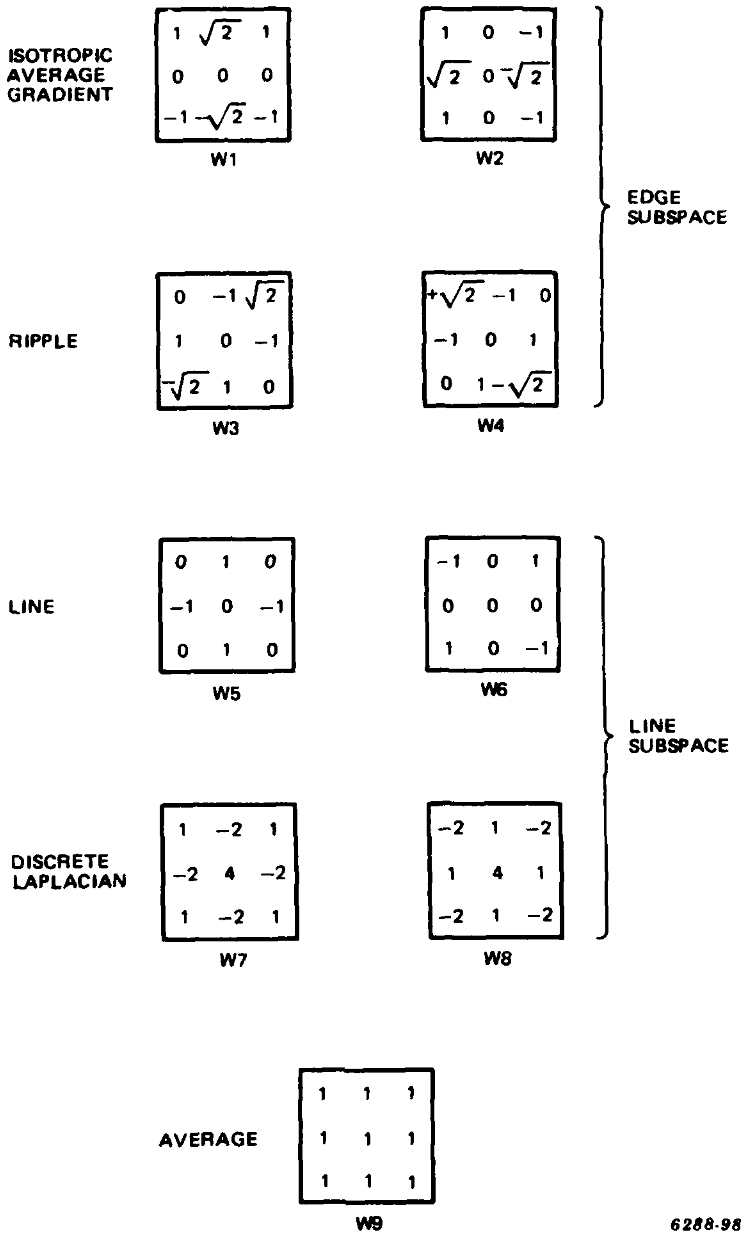

Figure 4-3. 9-Orthogonal Set of Edge Detection Basis Vectors

The point operator $O\{\cdot\}$ sums the four absolute values of the gradient arrays. The threshold decision is based upon a percentile of the histogram of the edge-enhanced array.

4.2 THINNING PROCESSING

The philosophy behind edge thinning, is that one would like to remove edge points without destroying the connectivity of the edges. The edge maps produced by using the edge detection schemes discussed above have had the tendency to produce thick edges. For the purpose of the border/edge points match computation, the edge response must be thinned.

The thinning algorithm proposed in the last report is a non-maximum suppression method[4,5]. This method needs the magnitude response as well as direction response of the thick edge map. Also the non-maximum suppression method applies four 5 by 5 pel masks in the edge-enhanced array with +45° resolution. In addition, from the investigation and implementation of different thinning algorithms by Professor T. S. Huang's group at MIT[3], the best thinning algorithm was produced by Reeves[6] at Purdue. Most of the other thinning algorithms tended to produce false artifacts in the edge maps. Reeves' algorithm is somewhat similar to edge detection, in that three 3 by 3 pel masks are used for thinning in each direction (ie. south, west, east, north). This algorithm is designed to thin the edge map by peeling off layers of edge points (map) iteratively until a single-pixel edge remains. A map where the edges were seven pixels wide would require three iterations of this process. The thinning masks are shown in Figure 4-4.

The Reeves' thinning algorithm is achieved by removing an edge point (designated X) only if one of the direction masks of Figure 4-4 exists. The "1"s indicate edge location and "Y"s are "don't care" locations. The operation is applied in sequence in the north, east, south, west directions respectively. That is, each edge point is tested against one of these masks. If the conditions of the mask are met, that edge point is removed. If the edge point does not meet one of the conditions of the mask in Figure 4-4, then the masks are

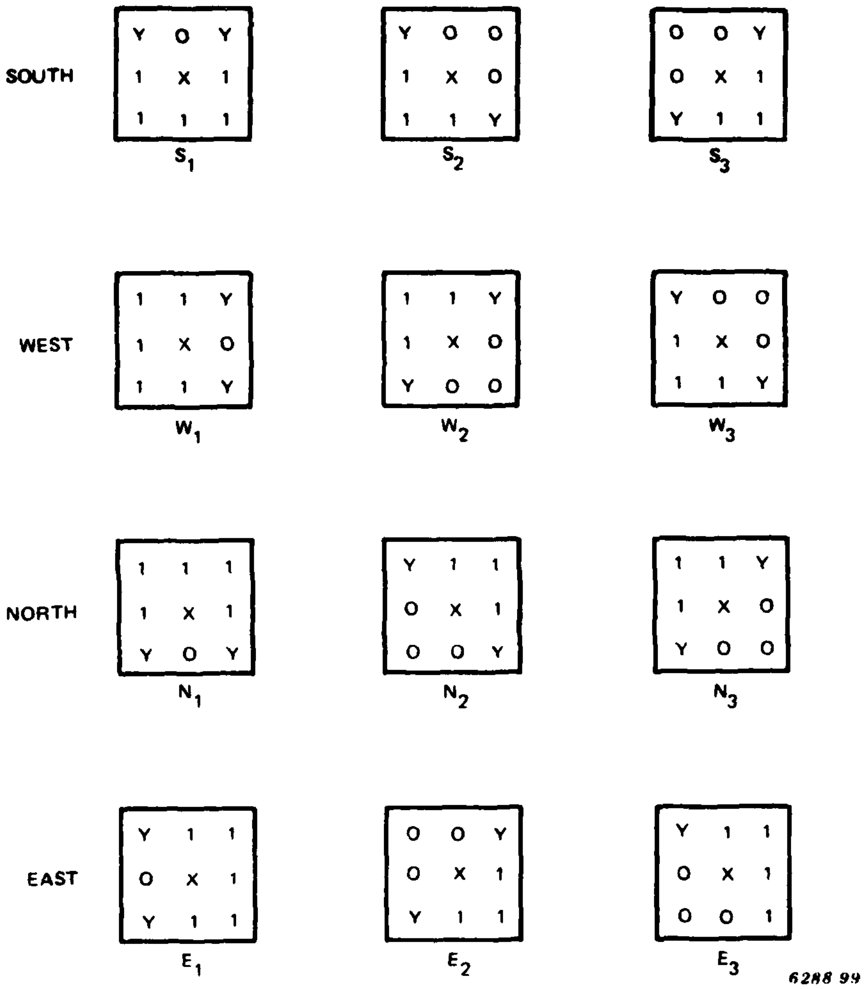

SOUTH

S_1

Y	O	Y
1	X	1
1	1	1

S_2

Y	O	O
1	X	O
1	1	Y

S_3

O	O	Y
O	X	1
Y	1	1

WEST

W_1

1	1	Y
1	X	O
1	1	Y

W_2

1	1	Y
1	X	O
Y	O	O

W_3

Y	O	O
1	X	O
1	1	Y

NORTH

N_1

1	1	1
1	X	1
Y	O	Y

N_2

Y	1	1
O	X	1
O	O	Y

N_3

1	1	Y
1	X	O
Y	O	O

EAST

E_1

Y	1	1
O	X	1
Y	1	1

E_2

O	O	Y
O	X	1
Y	1	1

E_3

Y	1	1
O	X	1
O	O	1

Figure 4-4. Reeves' Thinning Masks

rotated 90° clockwise and tested again. This operation continued until an edge point is removed, or the masks have been rotated a full 360°, (i.e., the edge point is only tested in the sequence of N_1, N_2, N_3, E_1, E_2, E_3, S_1, S_2, S_3, W_1, W_2, and W_3).

This algorithm has been implemented, and the thinned edge maps it produced are shown for each experimental result described in section 4.5.

4.3 THRESHOLD LEVEL SELECTION

The threshold level selection technique is a prime factor in image segmentation.

We have surveyed different threshold selection techniques such as global threshold selection based on gray level histogram, global threshold selection based on local properties, local threshold selection, and dynamic threshold selection[7 through 13]. We have selected a method using the local mean and standard deviation for automatic threshold selection. This method is particularly suitable for a small sized subimage input (i.e., 32 by 32 pel) for target silhouetting.

Using this technique candidate thresholds τ_i are given by

$$\tau_i = m + (i-4)\,\mu\sigma, \quad i = 0\text{-}3,\ 5\text{-}8$$

where m is the mean gray value of the subimage,

σ is the standard deviation of the subimage,

and μ is the adaptive constant determined by the curve shown in Figure 4-5.

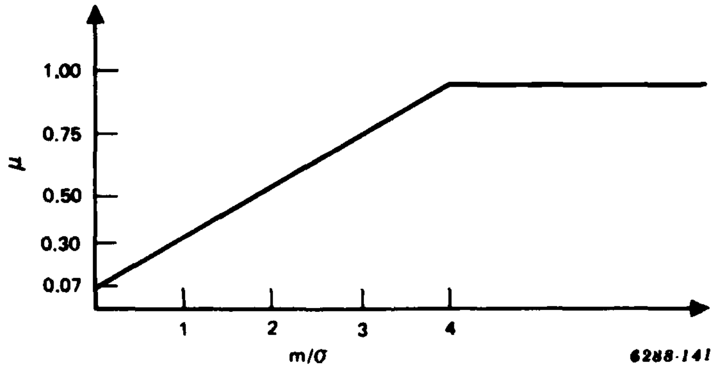

Figure 4-5. Adaptive Constant μ

The adaptive constant, μ, varies with effective contrast $[\frac{m}{\sigma}]$ of the subimage to ensure that trial thresholds are chosen throughout the entire subimage gray level range. The curve shown in Figure 4-5 was derived empirically from the statistics of target subframes taken from the NV&EOL data sets. The actual implementation of this method for threshold level selection does not need to compute the histogram but does need to compute the global mean and variance of the subimage.

When a smoothed image is thresholded at each gray level τ_i a family of binary image regions is obtained. These regions are the candidates for the target silhouette. In general, we wish to select the binary image B_k at a threshold level τ_k as the best representative of a true target silhouette under some predefined figure of merit.

4.4 FIGURE OF MERIT

A figure of merit is required in order to select the extracted binary image region that best corresponds to a true target silhouette. The selection of a member from the whole family of candidate binary images can be considered as a classification process. By computing features from the regions and using standard techniques, a discriminant function may be defined. This discriminant function can be interpreted as a figure of merit for any member of the set of candidate binary image regions. The member with the highest figure of merit is chosen as the true target silhouette. Members with a low figure of merit are discarded. The figure of merit used for each candidate region is measured by the percentage of region border points matching edge points in the thinned edge map.

4.5 IMPLEMENTATION, EXPERIMENTAL RESULTS, AND COMPARISONS

In this section we first discuss our current simulation and then present the experimental results. Next, we discuss the performance evaluation of the improved silhouetting system. We then show the experimental results of the other important algorithms and make comparisons.

4.5.1 Current Simulation and Implementation

The silhouetting system is shown in Figure 4-1. The 5 by 5 pel median filter suppresses random noise but does not blur edges. The central pixel value is replaced by the median value of the 5 by 5 pel window; the window slides one pixel, and the process is repeated. This operation is performed over the entire subimage. The edge detection system is implemented as shown in Figure 4-2. The spatial operators are the W_1, W_2, W_6, and W_7 masks. The point operator $O\{\cdot\}$ is performed by the summation of the absolute value of the gradient array of each mask. The threshold decision τ_{edge} is set to the 65th percentile of the edge-enhanced array histogram. The above algorithms produce the thick edge map. The thinning algorithm as shown in Figure 4-4 has been implemented to produce the thin edge map. This algorithm is iterative. We have found that in most cases only three passes were necessary to produce a thin edge map.

Unbiased estimates of the global mean and the variance of the subimages are computed and are used for the threshold level selection implementation.

A family of binary image regions are generated by encoding each region's gray level as 2^i if the subimage gray level is above the threshold level τ_i. Also, the border points of each candidate region are generated directly from these binary image regions. These algorithms are implemented with eight trail threshold levels in one pass.

4.5.2 The Performance Evaluation of the Improved Silhouetting System

We have implemented this system with 256 subimage sets from the NV&EOL data sets. The experimental results have been recorded in the Northrop PDP-11/34 computer system. We will show some typical sampled results in this section. The experimental results are shown in Figures 4-6 through 4-18.

We have adopted a subjective evaluation criterion to evaluate the performance of the target silhouetting system since there is no general unifying theory to evaluate the target silhouetting system. The subjective evaluation is measured by the percentage of the good silhouette output obtained in the experiment. From experimental results, we found that this system achieved more than 95 percent good target silhouettes from about 150 single target subimages. In addition, we also have observed that the experimental results are as good as those expected and are consistent with the theory discussed in section 2. Thus, the performance of this improved silhouetting system is excellent under this subjective evaluation criterion.

4.5.3 Implementation and Experimental Results of Other Important Algorithms

We have also implemented and revised the 2 by 2 pel edge detector associated with the non-maximum suppression thinning algorithm with even-space and mean-standard threshold selection techniques. This was done in order to complete the study of the silhouetting system and bridge the gap between the last report implementation and this report.

The details of these algorithms (excluding the mean-standard threshold selection techniques) are described in the last quarterly report. The format of the experimental results is shown in Figure 4-19, and the different algorithm system results are shown in Figure 4-20. (The format shown in Figure 4-19 corresponds to the images shown in each of the photographs in Figure 4-20.) The format of the progressive results is shown in Figure 4-21 and the progressive results themselves are shown in Figure 4-22 for the previously proposed silhouetting system.

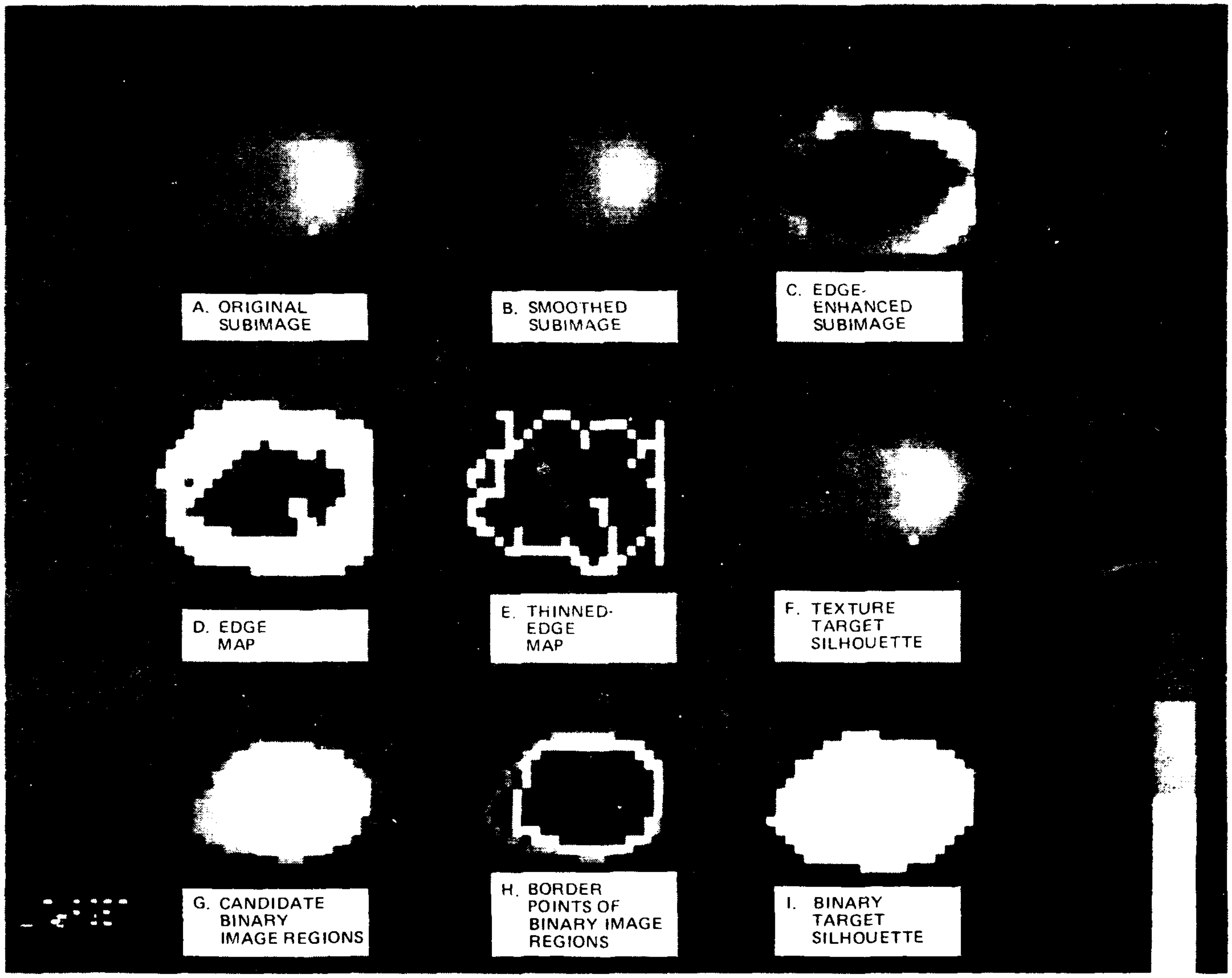

6288-142

Figure 4-6. The Experimental Result of Subimage 1

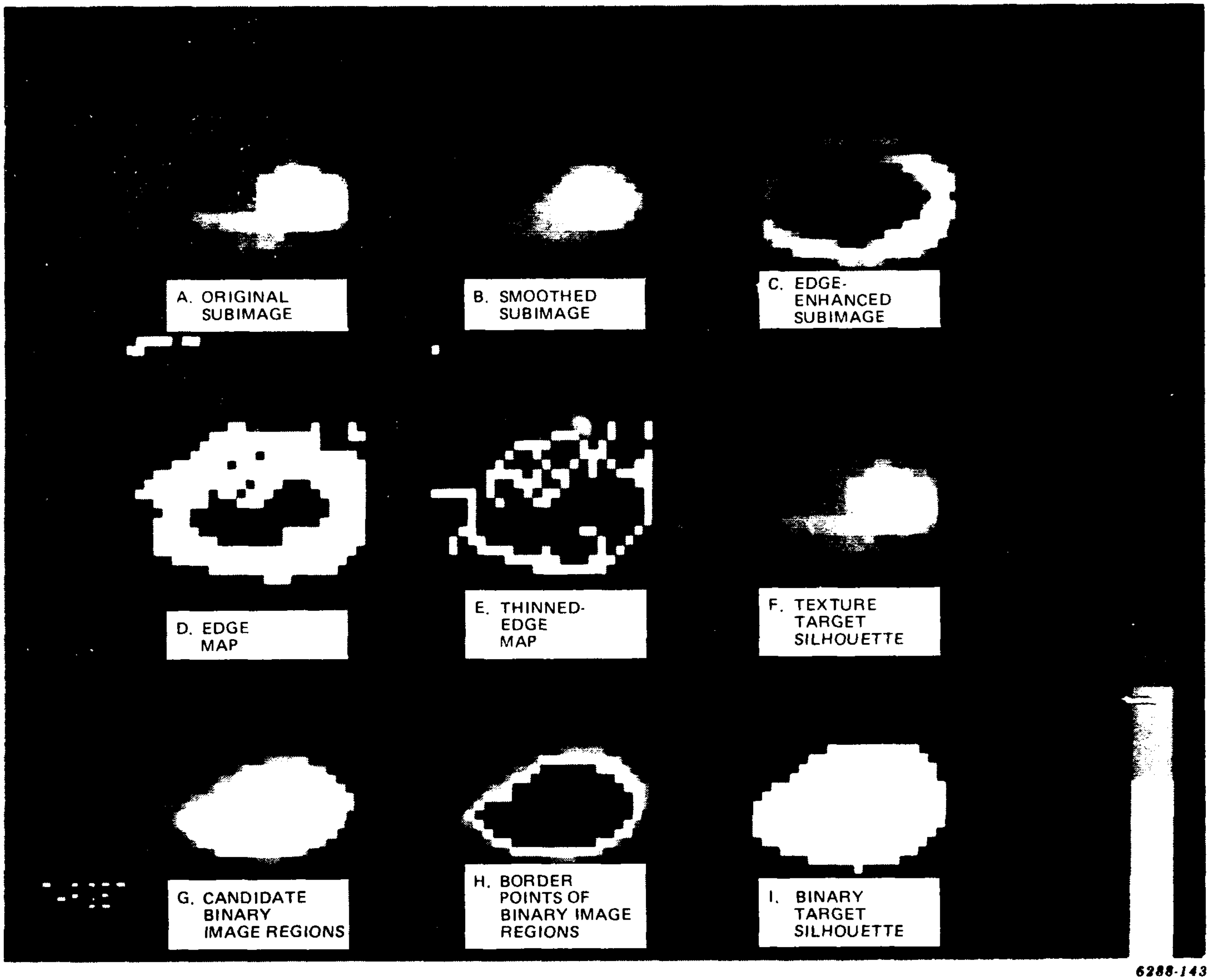

Figure 4-7. The Experimental Result of Subimage 7

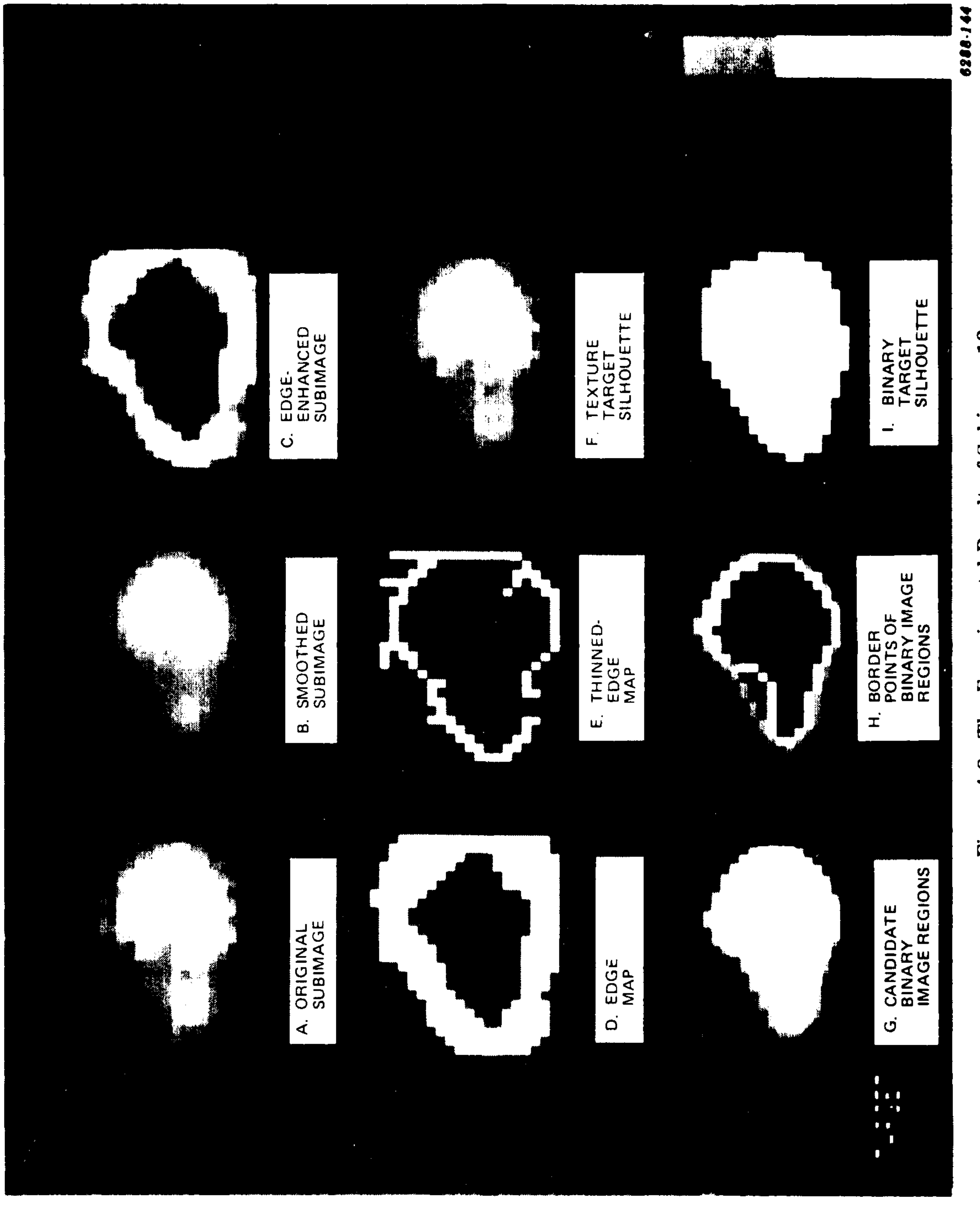

Figure 4-8. The Experimental Result of Subimage 13

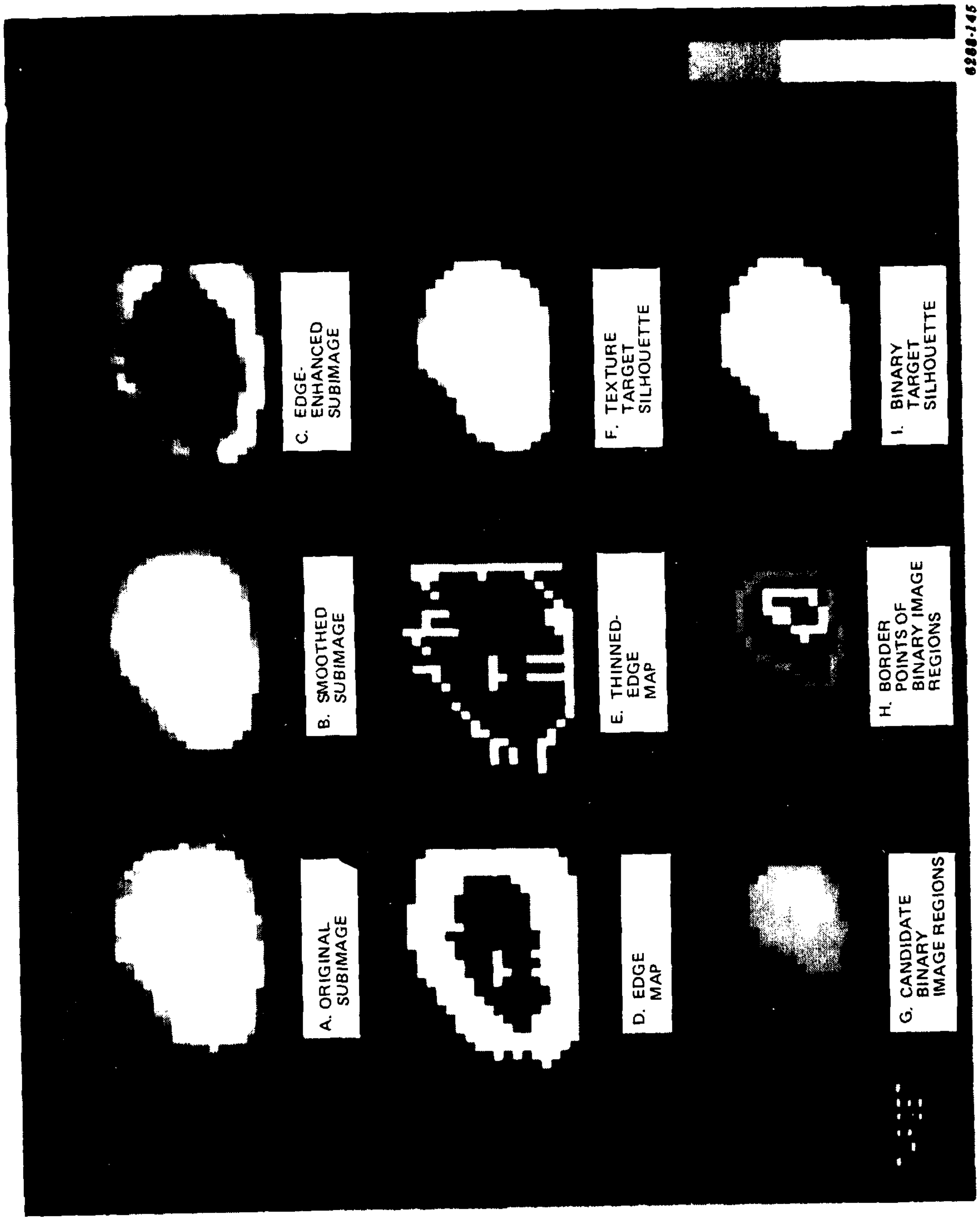

Figure 4-9. The Experimental Result of Subimage 43

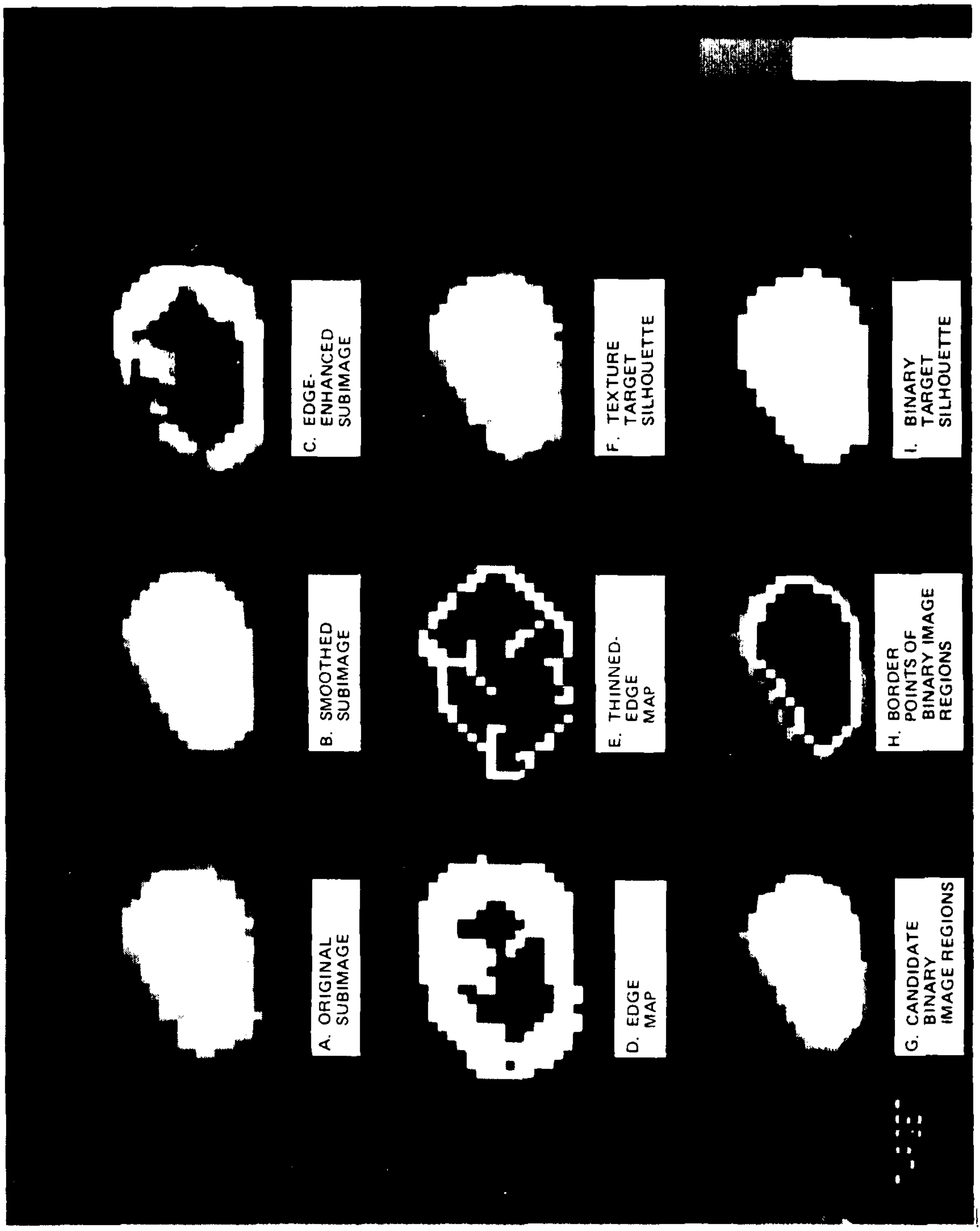

Figure 4-10. The Experimental Result of Subimage 46

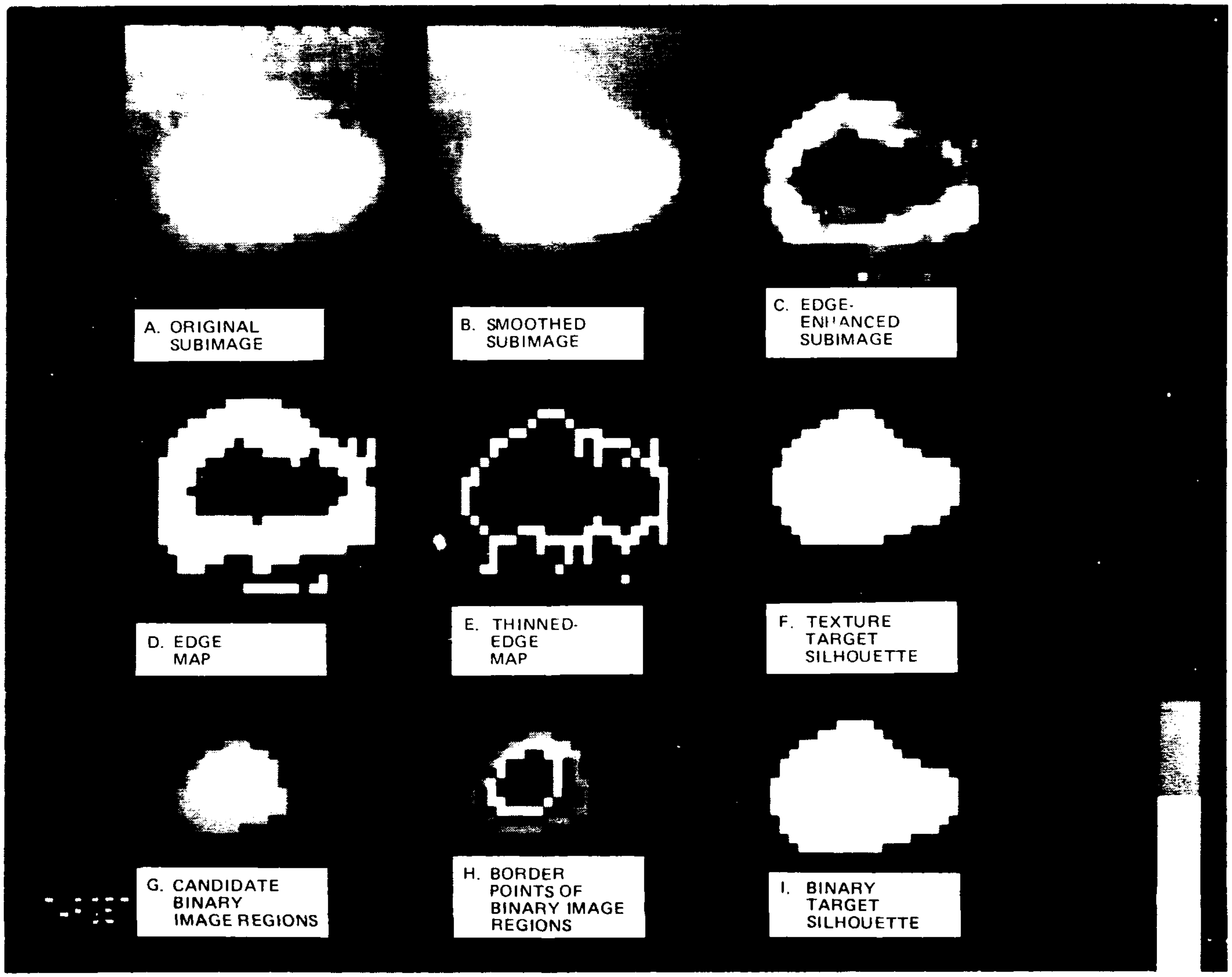

6288-147

Figure 4-11. The Experimental Result of Subimage 52

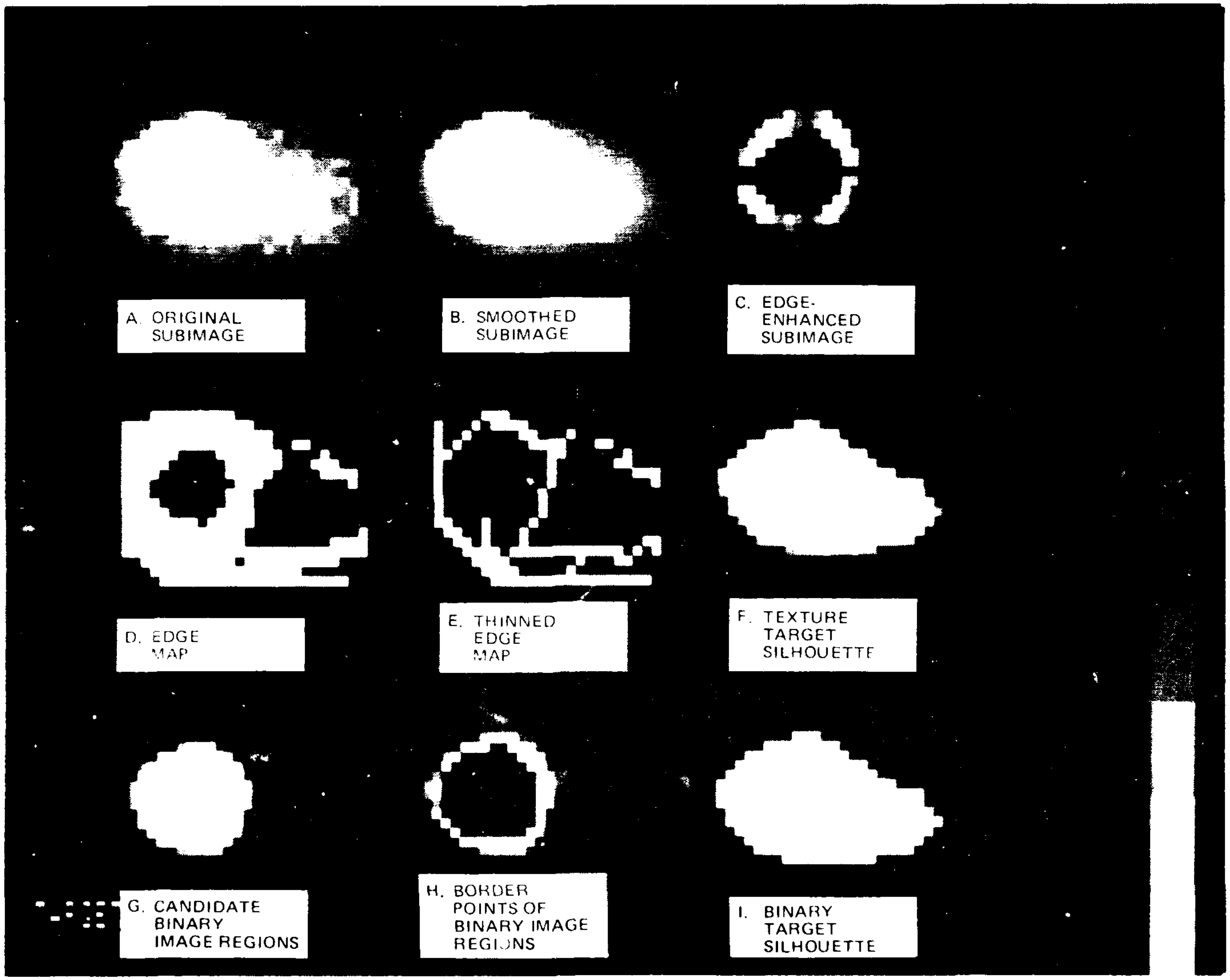

6288-148

Figure 4-12. The Experimental Result of Subimage 77

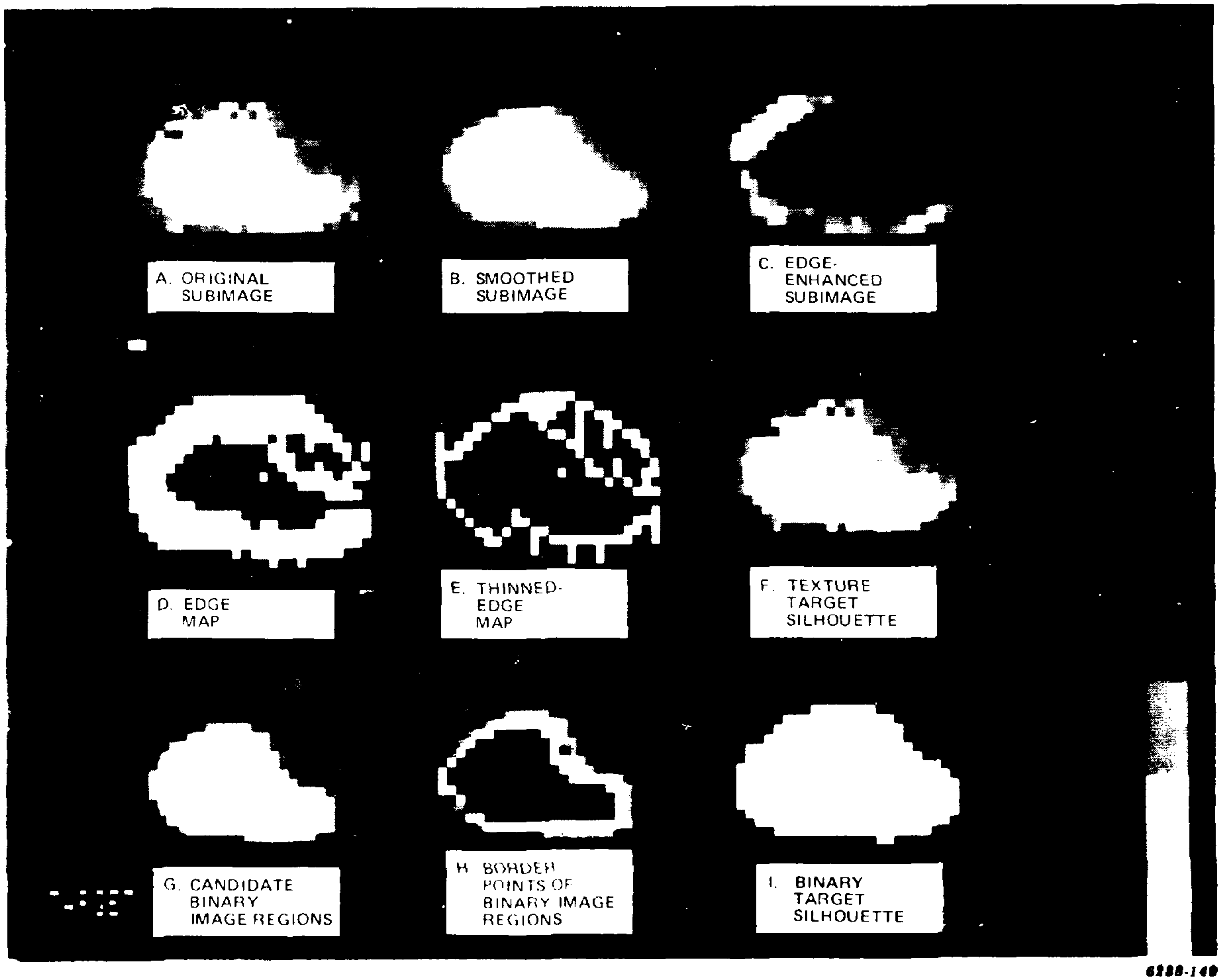

Figure 4-13. The Experimental Result of Subimage 87

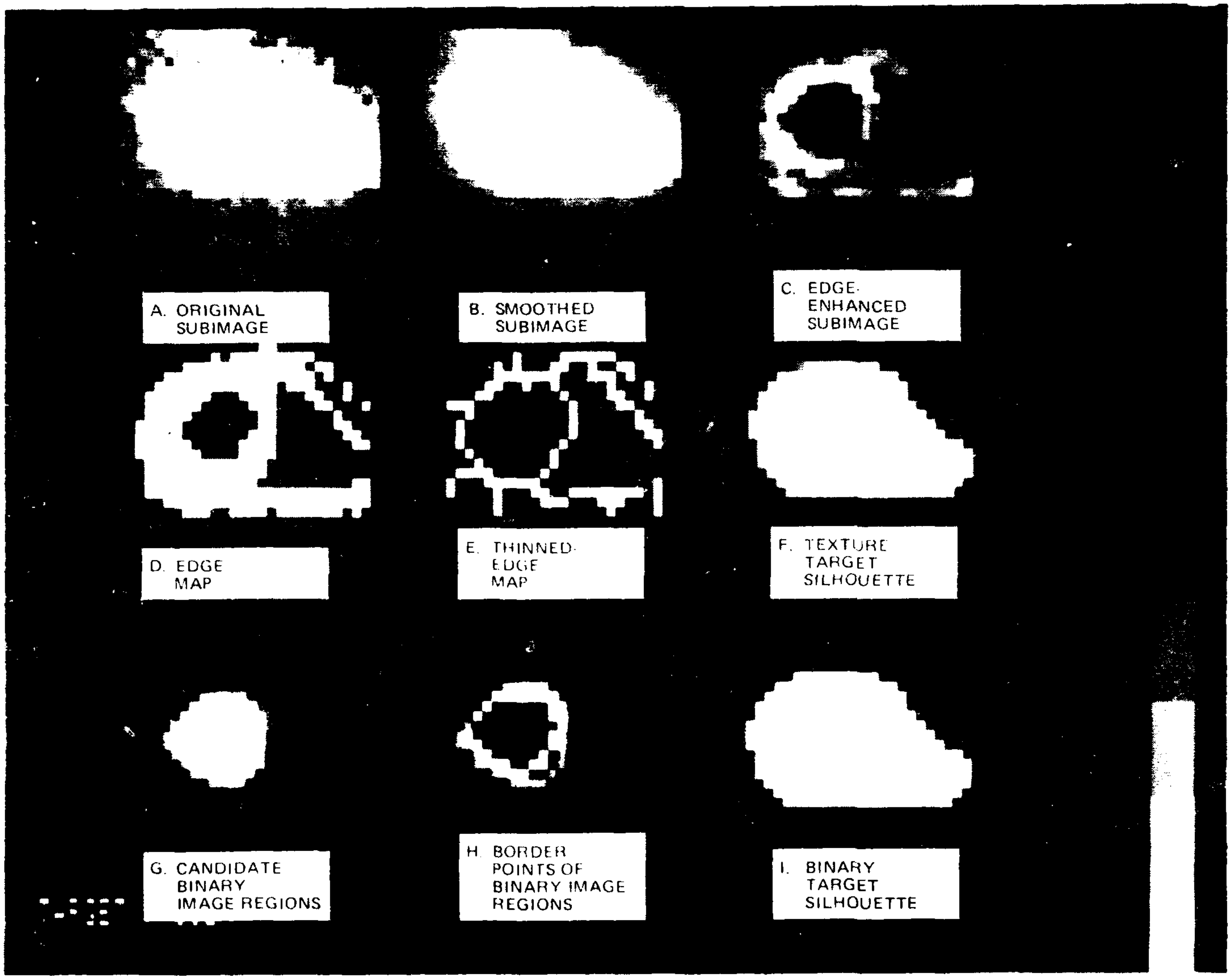

6288-180

Figure 4-14. The Experimental Result of Subimage 102

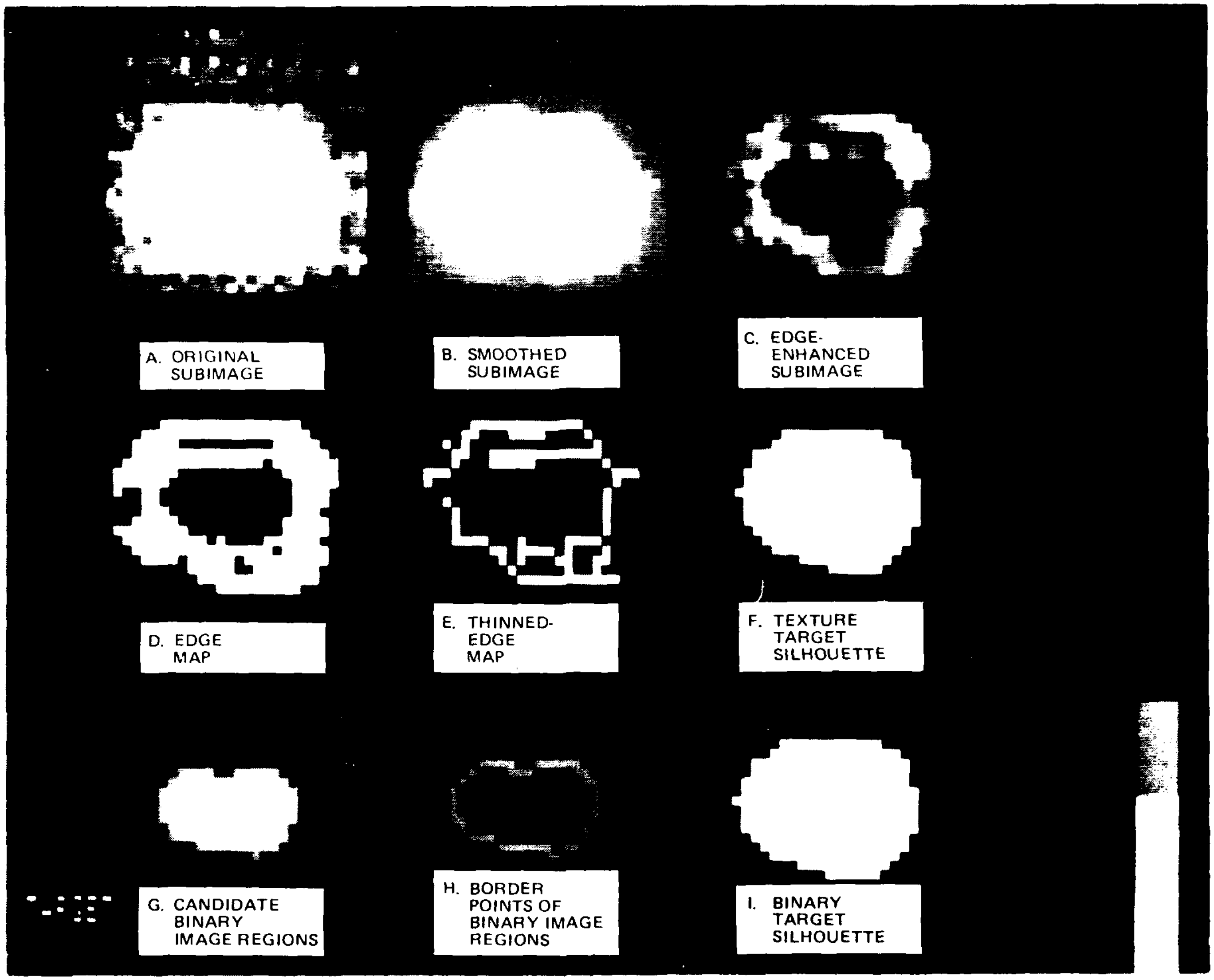

6288-151

Figure 4-15. The Experimental Result of Subimage 106

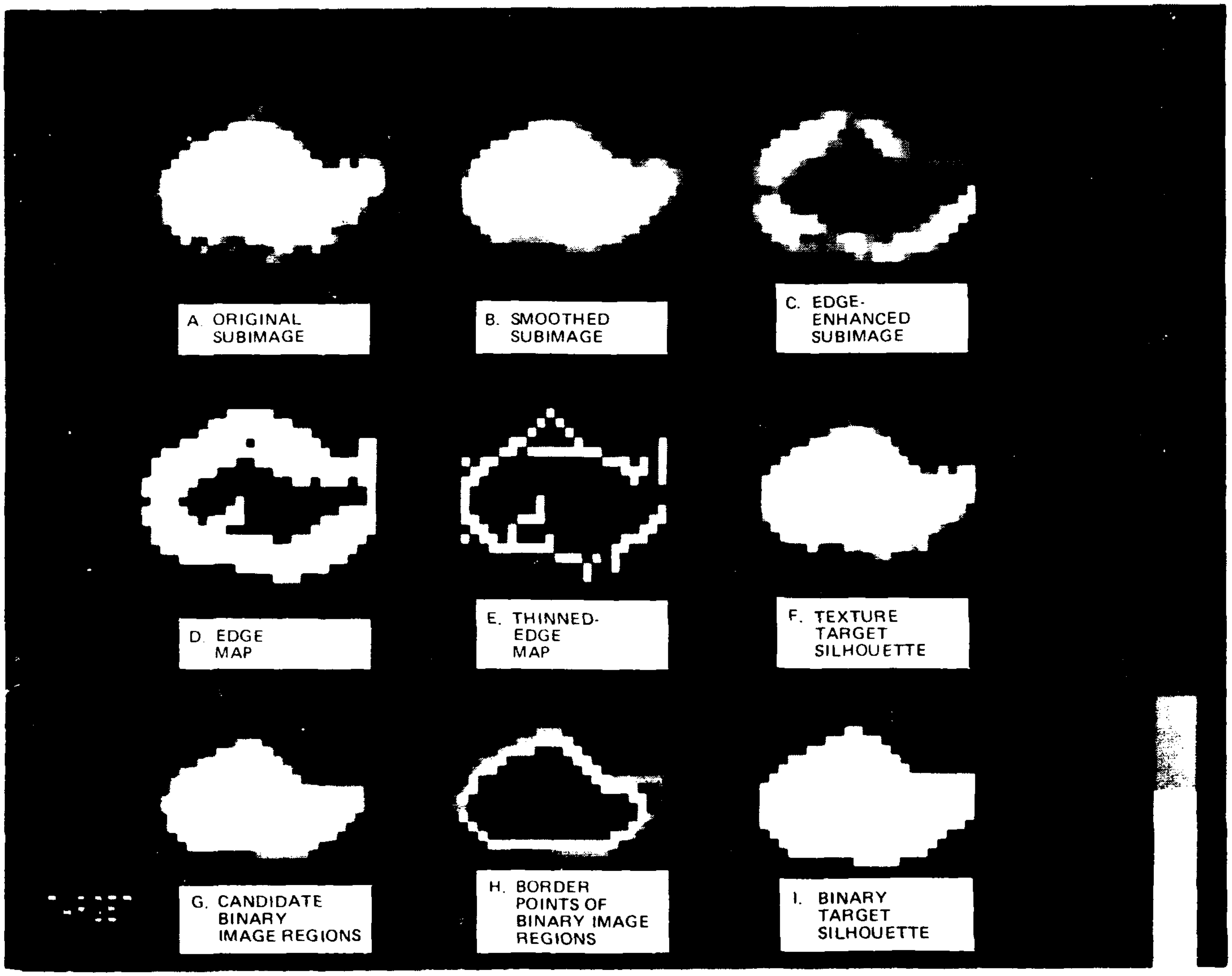

Figure 4-16. The Experimental Result of Subimage 109

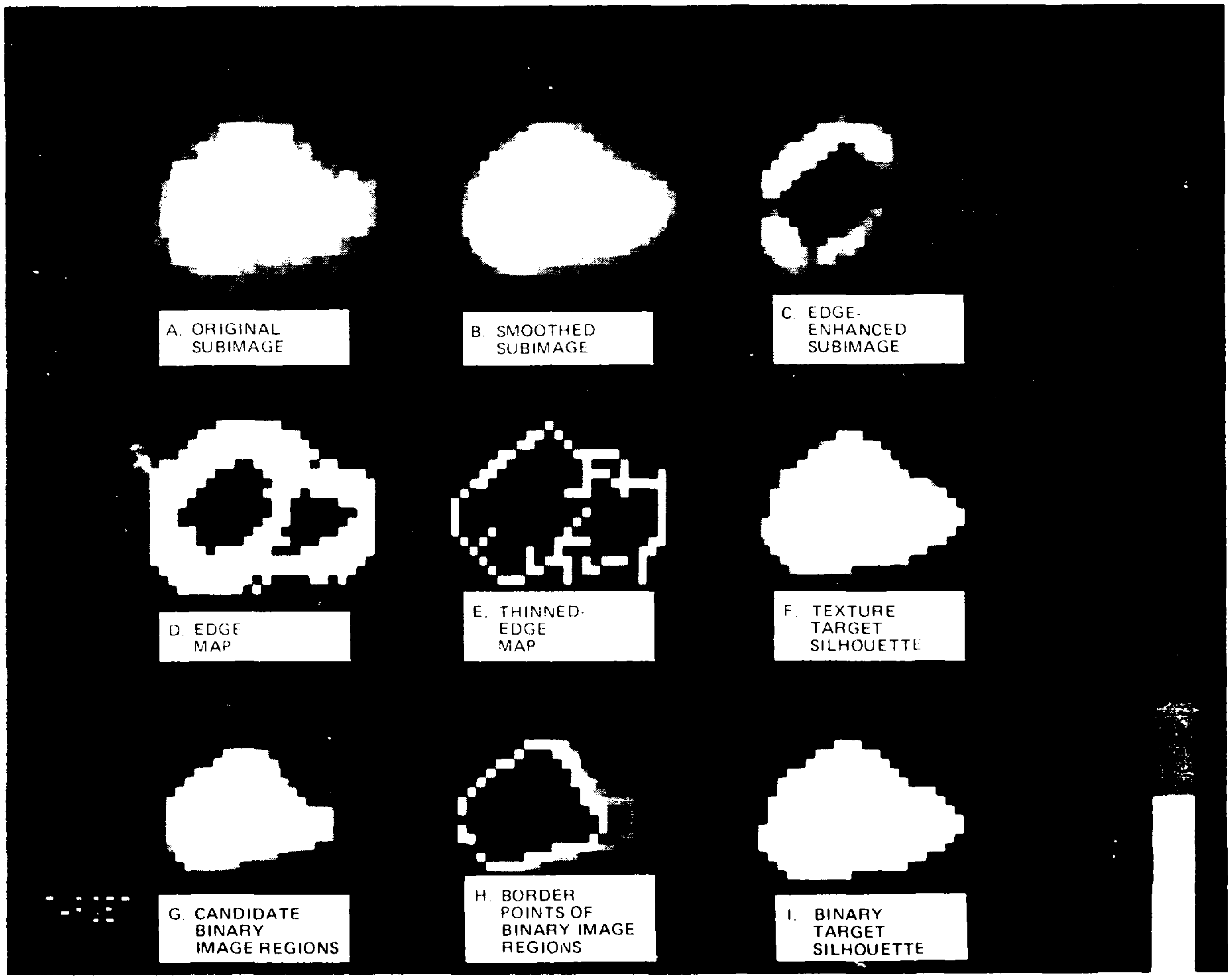

6288-153

Figure 4-17. The Experimental Result of Subimage 112

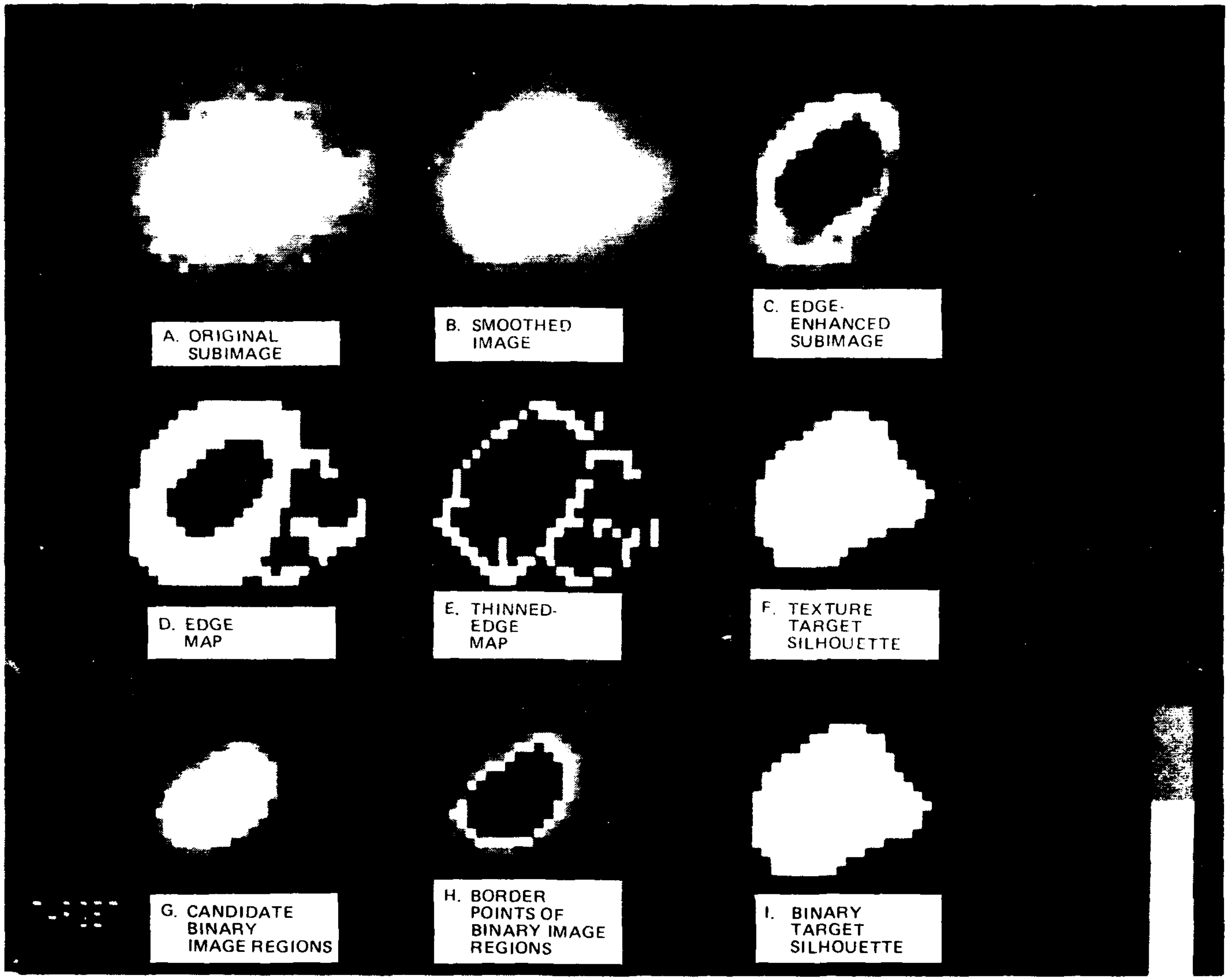

Figure 4-18. The Experimental Result of Subimage 115

From these experimental results, we can make the following observations:

a. The performance of the improved algorithm system (consisting of a 9-dimensional edge detector, Reeve's thinning processor and mean-standard deviation threshold system) is the best under subjective evaluation criterion. The output silhouette corresponds most closely to the true object silhouette.

b. The performance of the even-space threshold selection technique is inferior since this technique blindly selects a threshold level regardless of the kind of subimage input.

c. The thinned edge map generated by 2 by 2 pel edge detection associated with non-maximum suppression thinning algorithm is fragmented, broken, and noisy, while the improved edge detection associated with Reeves' thinning algorithm always gives a closed and clean thin-edge map.

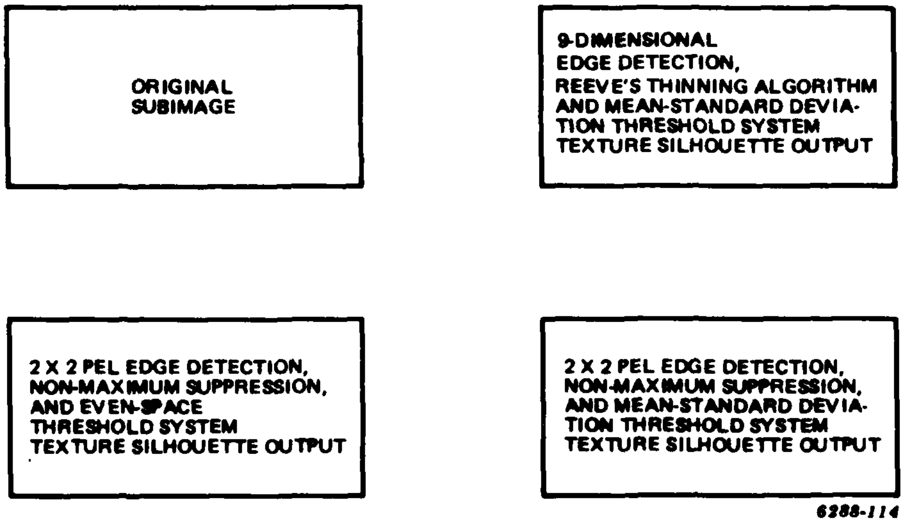

Figure 4-19. The Format of the Different Algorithm System Results

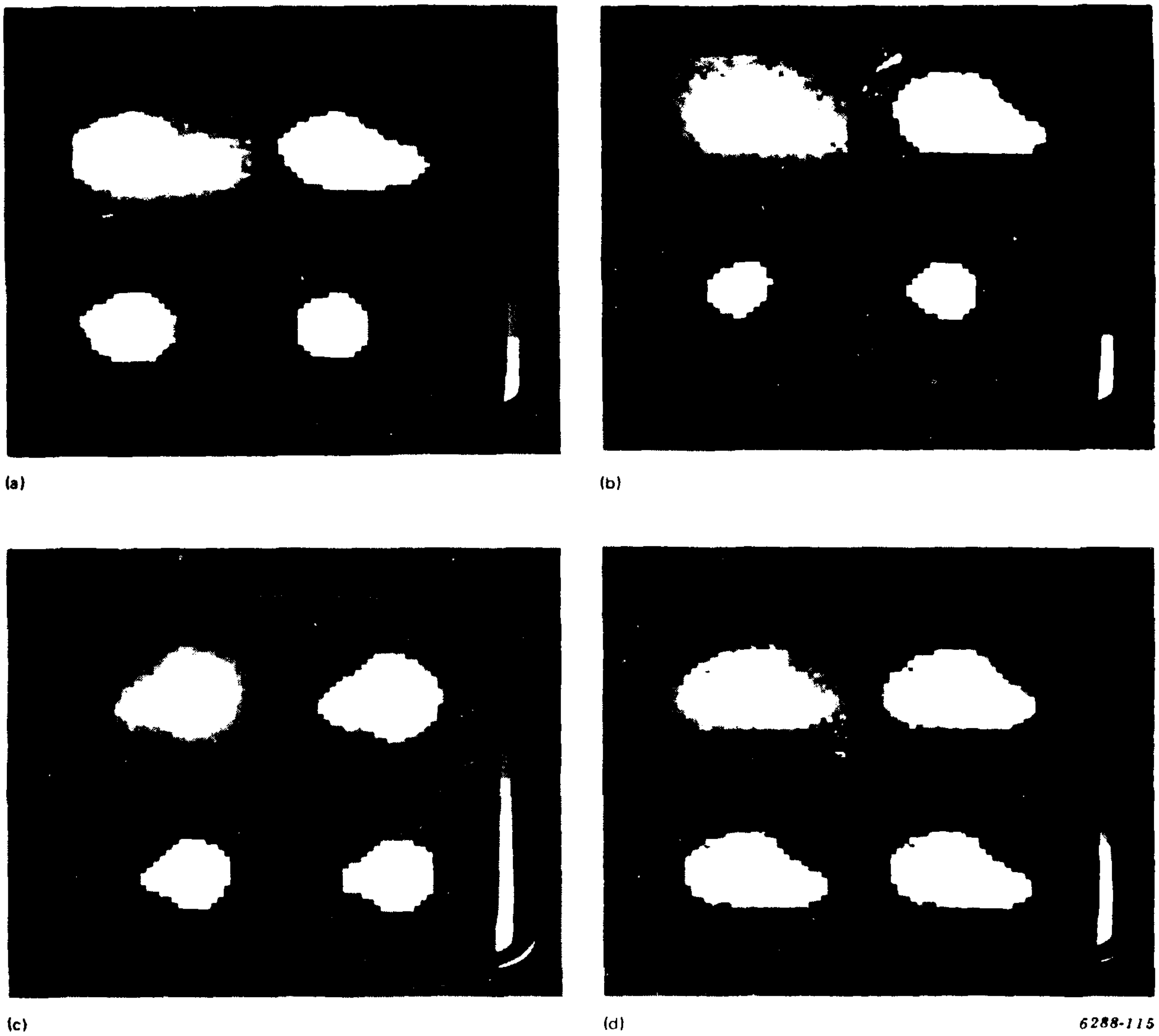

Figure 4-20. The Texture Silhouette Output of the Different Algorithm System

d. The 2 by 2 pel edge detection associated with non-maximum suppression thinning algorithm always gives a smaller silhouette output than the improved algorithm system does. This is also a kind of degradation since the silhouette of the improved algorithm system almost corresponds to the true defect silhouette by subjective judgment.

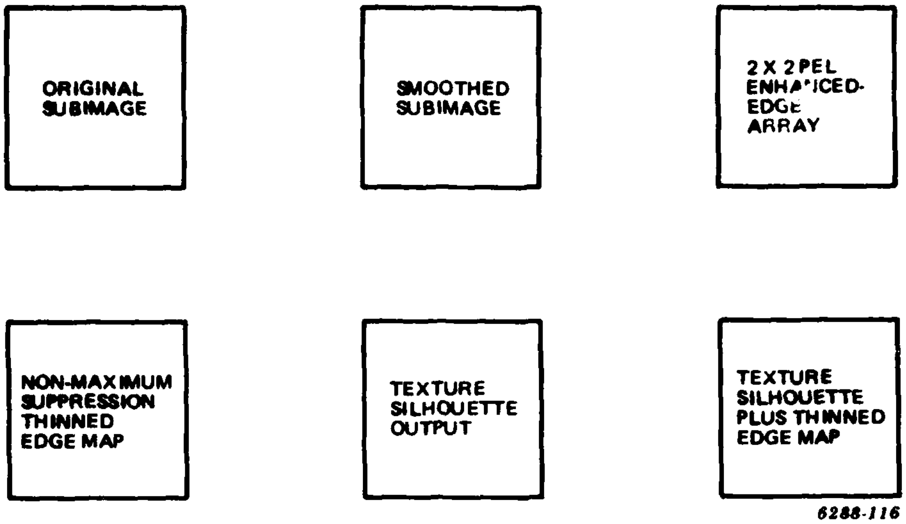

Figure 4-21. The Format of the Progressive Experimental Results with 2 by 2 Pel Edge Detection Associated with Non-Maximum Suppression Thinning Algorithm

4.6 SUMMARY

We have studied and implemented various algorithms of the target silhouetting system and have found good candidate algorithms for hardware modeling, simulation, and implementation.

The improved edge detection system, the Reeves' thinning algorithm, and mean-standard deviation threshold level selection techniques have produced superior silhouettes as compared to the other techniques. We also have implemented the target silhouetting system with efficient programs in Northrop's PDP-11/34 computer system.

Evaluation of the performance of the target silhouetting systems by subjective criterion is believed to be an appropriate, practical method. The improved silhouetting system is the best system under the above criterion.

However, the improved silhouetting system does suffer some deficiencies in its ability to handle multiple target regions. This drawback led to only a subset

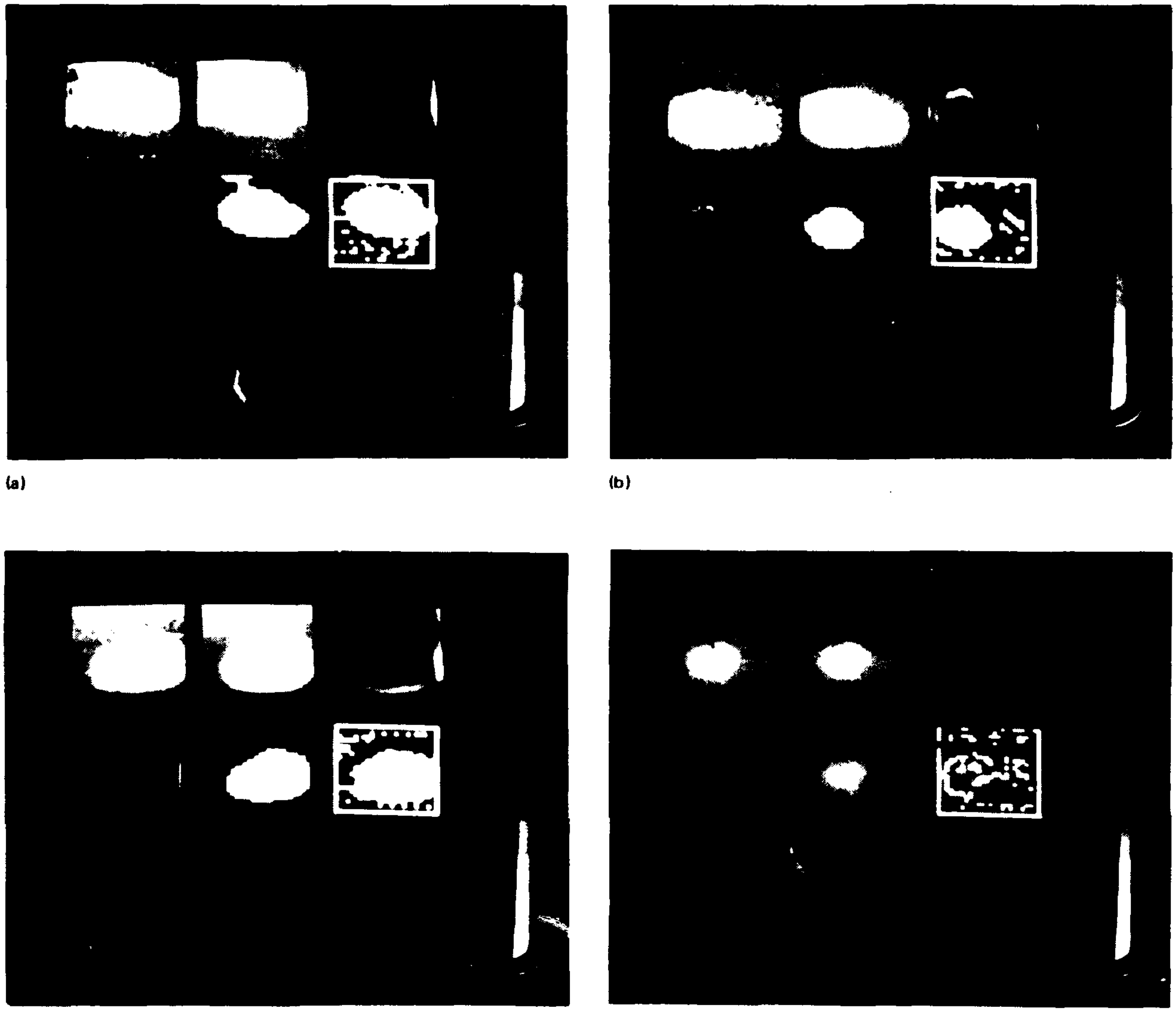

(a) (b) (c) (d)

6288-117

Figure 4-22. The Progressive Results of Silhouetting System with 2x2 Pel Detection Associated with Non-Maximum Suppression Thinning Algorithm

of the 150 subframes as being useful for input to the classification effort. This problem will be addressed in the next quarter's effort by the addition of a region labeling algorithm to identify separate silhouette regions and treat them individually.

4.7 REFERENCES

1. I. E. Abdou and W. K. Pratt, "Quantitative Design and Evaluation of Enhancement/Thresholding Edge Detector," proceeding of IEEE, Vol. 67, No. 5, May 1979.

2. W. Frei and C. C. Chen, "Fast Boundary Detection, A Generalization and a New Algorithm," IEEE trans. on computer, Vol. C-26, October 1977.

3. T. S. Huang and S. Krich, "Weapon Guidance Using Video Feedback," report of Lincoln Lab, MIT, 1978.

4. B. Deal _et al_, "Automatic Target Cuer First Quarter Report," Northrop Corp., 23 October 1979.

5. D. L. Milgram and A. Rosenfeld, "Algorithms and Hardware Technology for Image Recognition," _Final Report to NVL_, March 31, 1978.

6. A. P. Reeves, "A Systematically Designed Binary Processor," submitted for publication, 1978.

7. J. S. Weszka, R. N. Nagel, and A. Rosenfeld, "A Threshold Selection Technique," IEEE trans. on computer, Dec. 1974.

8. J. S. Weszka, "Survey: A Survey of Threshold Selection Techniques," Computer Graphics and Image Processing, Vol. 7, 1978.

9. D. L. Milgram, "Region Extraction Using Convergent Evidence," _Proceedings: Image Understanding Workshop_, April 1977, Science Applications, Inc.

10. A. Rosenfeld and A. C. Kak, _Digital Picture Processing_, Academic Press, 1976.

11. Y. Nakagawa and A. Rosenfeld, "Some Experiments on Variable Thresholding," Pattern Recognition, Vol. 11, pp. 191-204, 1979.

12. R. L. Kirby and A. Rosenfeld, "A Note on the Use of (Gray Level, Local Average Gray Level) Space as an Aid in Threshold Selection," IEEE Trans. on Systems, Man, and Cybernetics, Vol. SMC-9, No. 12, Dec. 1979.

13. E. M. Rounds, G. Sutty, "Segmentation Based on Second-order Statistics," Proceedings of SPIE, Vol. 205, Image Understanding System II, pp. 126-135, Aug. 29-30, 1979, San Diego, California.

SECTION 5

TARGET CLASSIFICATION

During this quarter the number of candidate feature sets was increased to include a modified Fourier set and four sets of moment features. Also, using the results of the silhouetting effort a data base of 58 targets has been examined. This section will present the features that were compared this quarter and the data base used as input. The performance of each set is evaluated and the optimal feature set has been selected for use in the ATC.

5.1 FOURIER FEATURE DEVELOPMENTS

The previous report showed that some of the Fourier features had definite characteristics that needed improvement. These factors were (a) mean distances between classes in feature space too small, (b) too much scatter for a particular class to be recognizable, and (3) features highly correlated. Therefore, new Northrop Fourier features have been developed.

Fourier I features (FD1 through FD5) are described in the appendix to the first quarter report, pages A-12 and A-13. They are retained in analysis strictly for comparative reasons.

Fourier II features differ from Fourier I by a correction factor which multiplies each feature as follows,

$$FD_i' = FD_i \cdot \mathrm{EXP}\ [1 - \mathrm{AREA}/\alpha].$$

where

FD_i' = revised Fourier feature
FD_i = old value
AREA = number of pels in candidate target
α = scale factor (approximately = 100)

Work completed last quarter showed this correlation removed some amount of feature correlation. Fourier II will be scored along with other candidates.

Fourier III features are a new set developed during the second quarter. They are described by reference to Figure 5-1 and Table 5-1.

The size invariance of descriptors NFD1 through NFD6 results because all features have compensating numerators and denominators. They are analogous to target geometric ratios in the x, y or spatial plane.

5.2 MOMENT FEATURES

Moment invariant features have been discussed in the literature by Hu, Dudani et al and Gonzalez and Wintz.[1,2,3]

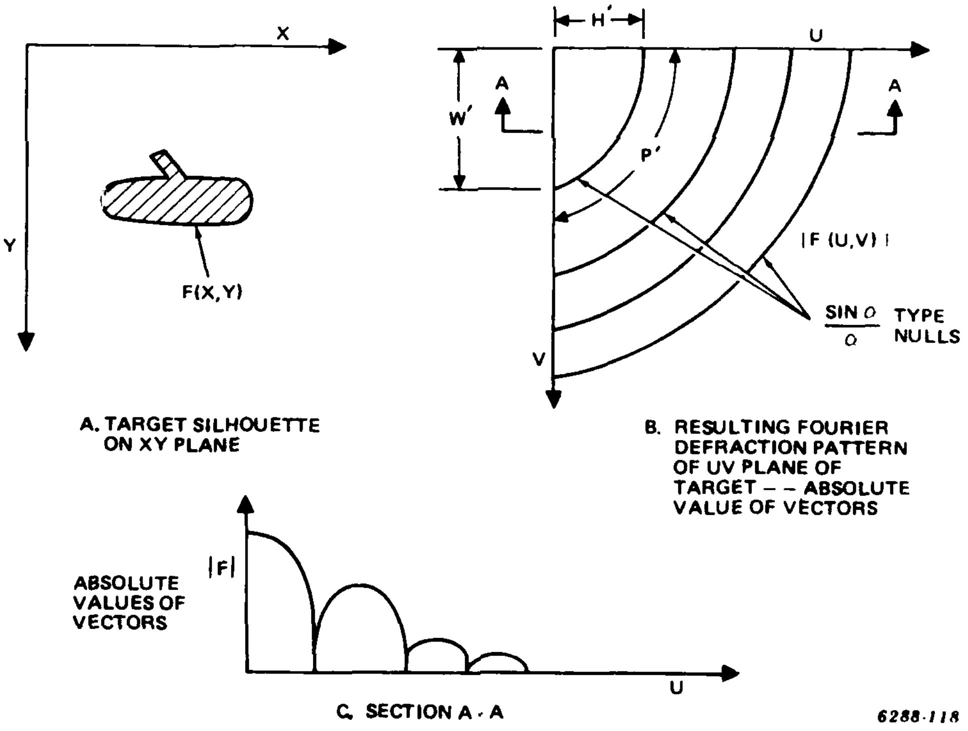

Figure 5-1. Mapping of Fourier III Features

Table 5-1. New Fourier Descriptors

1. NFD1 = h/w	h,w = sum of Fourier vectors are shown.
2. NFD2 = h*w/A	A = shaded area, sum of vectors in Figure 5-1.
3. NFD3 = h + w/P	P = sum of vectors, along perimeter of major null in Figure 5-1.
4. NFD5 = P^2/A	
5. NFD5 = SUMX16/SUMY16	SUMX16 = Sum of absolute magnitude vectors, on principal U axis.
6. NFD6 = SUMX16 * SUMY16/SUMX	SUM Y16 = Sum of absolute magnitude vectors, on principal V axis.
	SUMX = Sum of absolute magnitude vectors, entire positive Fourier plane.

They are composed of the central moments of a target silhouette or its boundary given by

$$\mu_{pq} = \frac{1}{N} \sum_{i=1}^{N} (u_i - \bar{u})^p \quad (v_i - \bar{v})^q$$

where,

μ_{pq} is the moment of the target silhouette

u_i, v_i are the image coordinates of the pels

$\bar{u}$, $\bar{v}$ are mean values of image coordinates u_i, v_i

N = no. of pels in target silhouette

p, q can be 1, 2 or 3

The moment features are given in Table 5-2.

Four feature sets are created using the moment features by preprocessing the input silhouette as shown in Table 5-3.

A binary silhouette is composed of 1's and 0's, while a textured silhouette substitutes image values for the 1's.

Table 5-2. Moment Features

$$MD1 = M_2/M_1^2$$

$$MD2 = M_3/M_1^3$$

$$MD3 = M_4/M_1^3$$

$$MD4 = M_5/M_1^6$$

$$MD5 = M_6/M_1^4$$

$$MD6 = M_7/M_1^6$$

where:

$$M_1 = (\mu_{20} + \mu_{02})$$

$$M_2 = (\mu_{20} - \mu_{02})^2 + 4\mu_{11}^2$$

$$M_3 = (\mu_{30} - 3\mu_{12})^2 + (3\mu_{21} - \mu_{03})^2$$

$$M_4 = (\mu_{30} + \mu_{12})^2 + (\mu_{21} + \mu_{03})^2$$

$$M_5 = (\mu_{30} - 3\mu_{12})\ (\mu_{30} + \mu_{12}) \cdot \left[(\mu_{30} + \mu_{12})^2 - 3(\mu_{21} + \mu_{03})^2\right]$$
$$+ (3\mu_{21} - \mu_{03})\ (\mu_{21} + \mu_{03}) \cdot \left[3(\mu_{30} + \mu_{12})^2 - (\mu_{21} + \mu_{03})^2\right]$$

$$M_6 = (\mu_{20} - \mu_{02}) \left[(\mu_{30} + \mu_{12})^2 - (\mu_{21} + \mu_{03})^2\right] + 4\mu_{11}\ (\mu_{30} + \mu_{12})$$
$$(\mu_{21} + \mu_{03})$$

$$M_7 = (3\mu_{21} - \mu_{03})\ (\mu_{30} + \mu_{12}) \cdot \left[(\mu_{30} + \mu_{12})^2 - 3(\mu_{21} + \mu_{03})^2\right]$$
$$- (\mu_{30} - 3\mu_{12})\ (\mu_{21} + \mu_{03}) \cdot \left[3(\mu_{30} + \mu_{12})^2 - (\mu_{21} + \mu_{03})^2\right].$$

Table 5-3. Input Conditions for Moment Features

Feature Set Name	Input Image Type
Dudani I	Binary Silhouette
Dudani II	Binary Silhouette Boundary
Dudani III	Textured Silhouette
Dudani IV	Textured Silhouette Boundary

5.3 UNIVERSITY OF MARYLAND FEATURES

The feature set labelled Maryland I is defined in the first quarter report.

The Maryland II feature set differs from Maryland I in that feature no. 3, 4, 6 and 7 are changed as shown in Table 5-4. Normalization areas N were altered or dropped.

Table 5-4. Difference Between Maryland I and Maryland II

Feature No.	Maryland I	Maryland II
3	$\left(X_{AVE} \cdot Y_{AVE}/N\right)\frac{1}{N}$	$X_{AVE} \cdot Y_{AVE}/N$
4	$\left(\frac{X_{AVE}}{\sqrt{N}} + \frac{Y_{AVE}}{\sqrt{N}} - 4\right)\Big/ P$	$\left(X_{AVE} + Y_{AVE} - 4\right)/ P$
6	$\lvert SXY/R^2 \rvert \cdot N$	$\lvert SXY/R^2 \rvert$
7	$\frac{N^2 (SXY)^2 - SX^2 SY^2}{R^4}$	$\frac{(SXY)^2 - SX^2 SY^2}{R^4}$

5.4 DATA BASE

The data base used to evaluate the performance of the feature sets was made from a subset of the data base used to test the silhouetter. The target silhouettes used for classification are shown in Figure 5-2. There are tanks, Armored Personnel Carriers (APC's), and jeeps in this target set.

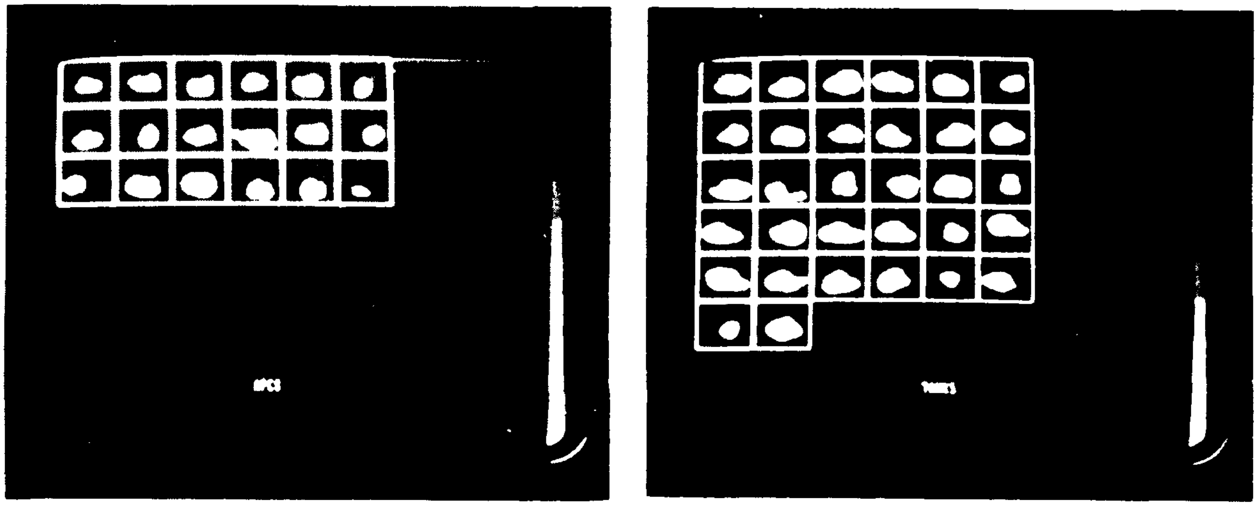

APC'S TANKS

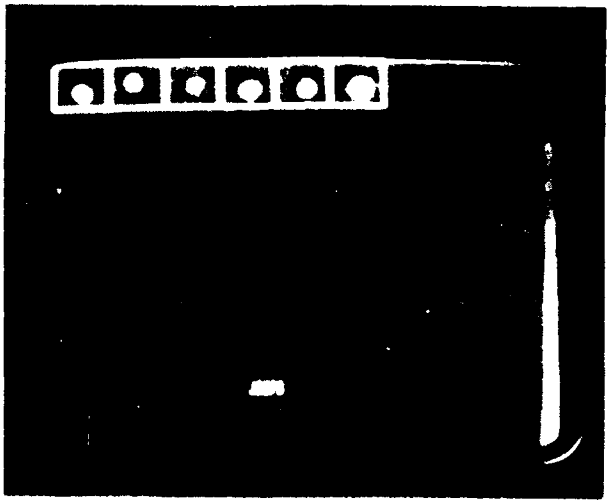

JEEPS

6288-121

Figure 5-2. Target Silhouettes

5.5 FEATURE SET EVALUATION

Last quarter we described a method of cluster analysis whereby the performance of any feature set can be evaluated: first, find those significant clusters of training targets in feature space; second, name each cluster by its majority true membership; third, classify all training targets in every cluster according to that clusters' name. This procedure has the advantage of yielding a continuous function-relating performance (PR=probability of recognition) to a relaxation criteria controlling the formation of clusters. It has the disadvantage of being time-consuming to run on a computer. Moreover, since this method is new to the industry it does not allow for easy comparisons of previously published results.

For this report then, we obtain point estimates of probability of recognition from a k-nearest neighbor classifier using the U-method. In this method one sample from the training set is initially chosen for the test set, and the remaining samples are assigned to the training set. The classifier then runs with the removed sample used for testing performance. Next, the test sample is assigned to the training set, and a new sample is removed from the training set and used for testing. The process continues until all members of the training set have served as test points. This procedure results in perhaps the most statistically significant measure of performance.[4]

Classification is performed with the k-nearest neighbor method by measuring distances in feature space and determining classification according to the population of the classes or neighbors about the test point. The robustness of any feature set may be determined by counting the number of neighbors out of k about the test sample that belong to the correct classification of that sample.

Our evaluation, then, is based on finding (a) the best performing target feature set in terms of probability of recognition, and (b) that good-performing feature set which promises to yield the most robust classifier.

5.5.1 Probability of Recognition (PR)

Our analysis was exhaustive for k=1,2,..,5, for each of the 9 feature sets taken as a whole in multidimensional euclidean feature space, and for each single feature in all feature sets.

As can be seen from Table 5-5, the best feature set was Maryland II. For all targets, a PR = 72.4 and for tanks a PR = 81.2 were obtained.

The best single feature from each set is shown in Table 5-6. For both targets and tanks, feature 9 from the Maryland I set ranked first in performance. In particular, it is noteworthy that this single target feature performs about as well as the entire set of 10 Maryland features combined.

5.5.2 Classification Performance as a Function of K

Figures 5-3 and 5-4 show the performance of each feature set as a function of k. A feature set that was robust statistically would tend to have a flat or slightly positive slope in these figures.

Table 5-5. Feature Set Performance (Multidimensional K-Nearest Neighbor Classification)

	All Targets		Tanks	
Rank	Feature Set	PR (%)	Feature Set	PR (%)
1	M2	72.4	M2	81.2
2	D2	67.2	D1	81.2
3	M1	62.1	D2	78.1
4	D1	58.6	F3	75.0
5	D4	58.6	M1	68.7
6	F3	56.9	F1	68.2
7	F2	53.4	D4	65.6
8	F1	53.4	F2	65.6
9	D3	44.8	D3	56.2

Table 5-6. Best Single Feature Performance (K-Nearest Neighbor Classification)

Rank	All Targets				Tanks			
	Feature		k	PR (%)	Feature		k	PR (%)
	Set	ID			Set	ID		
1	M1	9	1	69.0	M1	9	1	81.2
2	M2	9	1	69.0	M2	9	1	81.2
3	F2	3	3	58.6	D4	1	1	71.9
4	D1	5	2	56.9	F2	3	1	71.9
5	D3	4	4	55.2	D1	4	1	68.7
6	D4	1	1	51.7	F1	4	1	68.7
7	D2	4	3	51.7	F3	2	1	65.6
8	F1	4	1	51.7	D3	5	1	62.5
9	F3	5	1	51.7	D2	4	1	59.4

In Figure 5-3 the three Fourier measures (F1, F2, F3) drop to near-chance levels of performance with increasing k, suggesting that regardless of how high an initial point estimate of PR was, in the long run that estimate should not be relied on. The function for the Maryland set, on the other hand, tend mostly to be flat.

Figure 5-4 shows the same stability for the Dudani feature set as can be seen for the Maryland set.

Therefore, we conclude that use of Fourier features would produce less robust target classification than either Dudani or Maryland features.

5.6 CONCLUSION AND PLANS

The performances of nine candidate feature sets have been compared. The feature set with the best performance was Maryland II. Since this feature set is also one of the easier sets to compute as well, it has been selected as the ATC feature set.

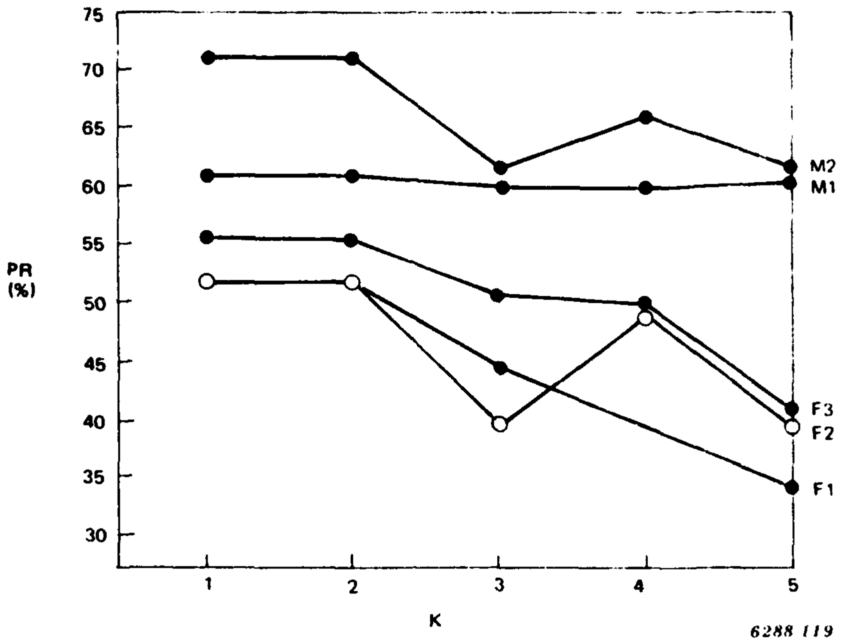

Figure 5-3. Classification Performance of Maryland versus Fourier Features as a Function of K

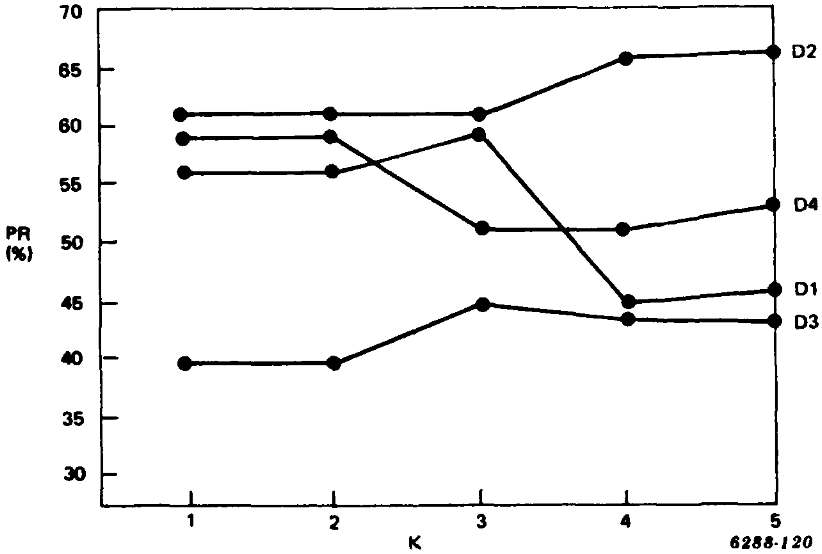

Figure 5-4. Classification Performance of Dudani Features as a Function of K

During the next quarter, the feature set computations will be revised for microprocessor efficiency. Also, the structure of the decision regions in feature space will be examined to identify optimal decision rules. This last effort will increase the PR to be more in line with the design goal of PR ≥ 0.9.

5.7 REFERENCES

1. M. K. Hu, "Visual Pattern Recognition by Moment Invariants," IRE Trans. Info. Theory, Vol. IT-8, pp 179-187, Feb. 1962

2. S. A. Dudani, K. J. Breeding, and R. B. McGhee, "Aircraft Identification by Moment Invariants," IEEE Trans. Comput., Vol. C-26, pp 39-45, Jan. 1977

3. R. C. Gonzalez and P. Wintz, "Digital Image Processing." Reading, Mass. Addison-Wesley, 1977.

4. Lachenbruch & Mickey, Estimation of Error Rates in Discriminant Analysis. Technometrics, Volume 10, pages 1-11, 1968; Fukunaga & Kessle, Estimation of Classification Error, IEEE Trans. on Comput., C-20, pages 1521-1527, 1971.

SECTION 6
SCAN MIRROR POSITION SENSOR

The requirements for a scanner mirror position sensor were stated in the first quarter report. At that time, the Hall-effect transducer was used which is a part of the scan mirror drive electronics. It was also noted that there would be a requirement for a signal-to-noise ratio of approximately 80 db. The Hall-effect transducer approach is quite risky for the following reasons: (1) the high possibility of noise contamination of the signal, (2) distortion that might result from attempting to filter the signal, (3) the requirement to modify the existing common module Forward-Looking Infrared (FLIR) to gain access to the required signals, and (4) the possibility of interfering with FLIR operation by introduction of noise into the scan mirror drive electronics. Therefore, effort has been redirected toward the use of a lateral-effect photodiode detector as a mirror position transducer.

6.1 LATERAL-EFFECT PHOTODIODE DETECTOR CONCEPT

The lateral-effect photodiode consists of an active surface of approximately 4 mm by 30 mm, a bias junction, and two output terminals. The current from the output terminals is proportional to the intensity of the incident light and the position of the light spot, with respect to the center of the diode. A simplified equivalent circuit of the diode is shown in Figure 6-1. The diode may be considered as a potentiometer of total resistance, R, with a current source, I_d, in the potentiometer arm. The value, K, is the ratio of the selected resistance (as determined by the potentiometer arm setting) to half the total resistance. In the actual diode, K is the ratio of the light spot position, measured from the center of the diode active surface, to half the total length of the active surface. The current, I_d, is proportional to the total intensity of the light spot incident on the active surface of the diode.

From the simplified equivalent circuit, it can be seen that the output currents are:

$$I_1 = \frac{I_d((1 + K)R + 2R_L)}{2(2R_L + R)} \quad \text{, and}$$

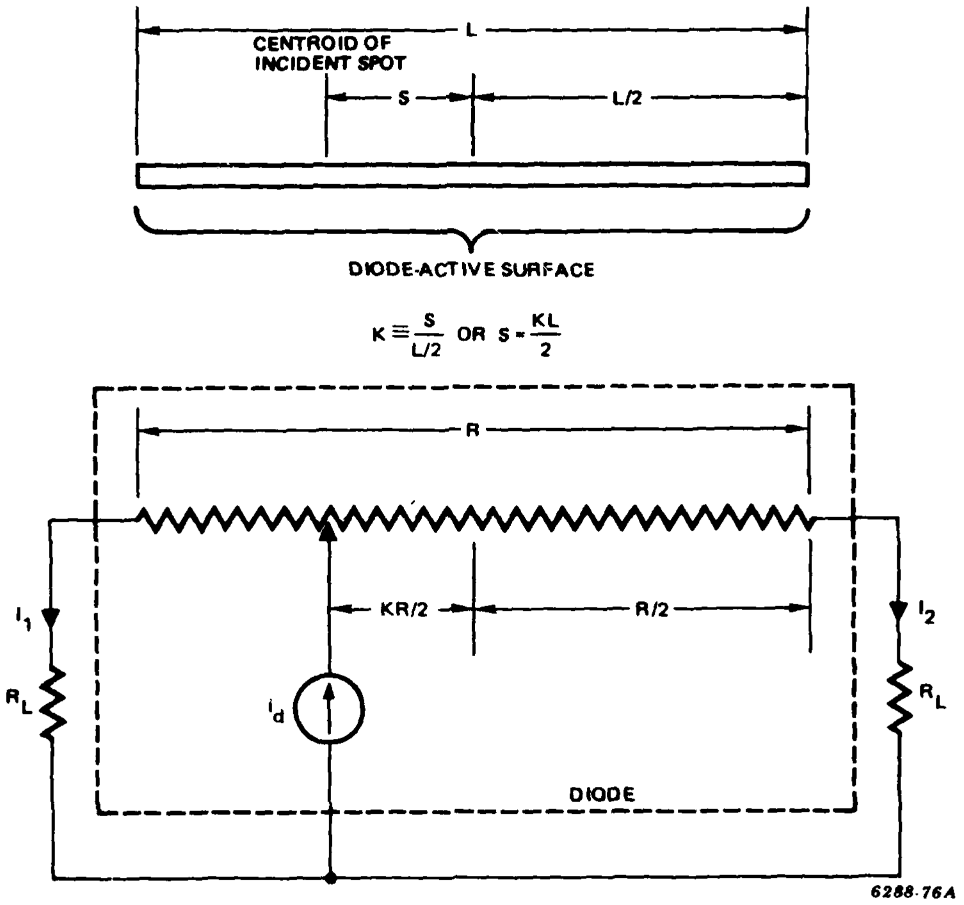

Figure 6-1. Lateral-Effect Photodiode--Simplified Equivalent Circuit

$$I_2 = \frac{I_d((1 - K)R + 2R_L)}{2(2R_L + R)}$$

R_L is the load impedance (i.e., input impedance of the external measurement circuit).

6.2 SIGNAL PROCESSING

Each current output from the diode is fed into a transconductance amplifier, typical of the schematic diagram shown in Figure 6-2. The transconductance

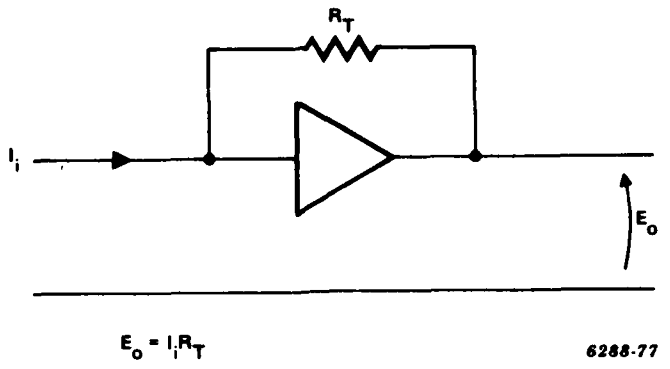

Figure 6-2. Transconductance Amplifier--Output Voltage Proportional to Input Current

amplifier produces a voltage output which is proportional to the input current, with the scale factor being controlled by the value of the feedback resistance. The transconductance amplifier also exhibits a very low input impedance, typically less than one ohm. The characteristic impedance, R, of the lateral-effect diode is relatively high, typically on the order of 10,000 ohms. From the expressions just given for the output currents, it can be seen that as R_L approaches zero, with respect to R, the currents become:

$$I_1 = \frac{I_d(1+K)}{2}, \text{ and } I_2 = \frac{I_d(1-K)}{2}$$

The corresponding voltages from the transconductance amplifiers become:

$$E_1 = \frac{I_d(1+K)R_t}{2}, \text{ and } E_2 = \frac{-I_d(1-K)R_t}{2}$$

The outputs from the transconductance amplifiers are then routed to the inputs of a sum amplifier and a difference amplifier, each of which includes a phase reversal to eliminate the negative sign in the immediately previous equations. The output from the sum amplifier will then be:

$$E_s = E_1+E_2 = I_dR_t$$

and the output from the difference amplifier becomes:

$$E_d = E_1-E_2 = KI_dR_t$$

Next, these two signals are routed to a pair of differential cable drive amplifiers.

In the present design of the position sensor, the amplifiers, along with the lateral-effect photodiode, are physically mounted on a common circuit board, and the entire assembly is contained within a shielded enclosure mounted directly onto the scan-mirror mechanical assembly, as illustrated in Figure 6-3. The differential cable drivers control a shielded and sheathed cable between this enclosure and the enclosure containing the remainder of the multiplexer electronics, where the signals are received on a pair of differential receivers.

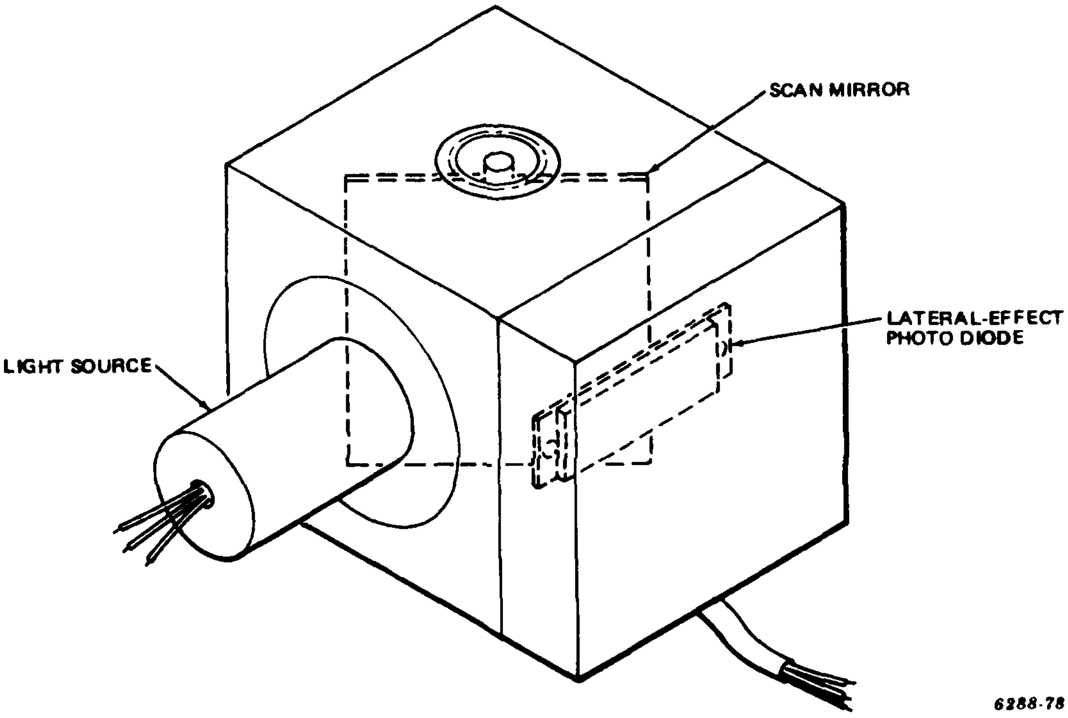

Figure 6-3. Physical Mounting of Lateral-Effect Photodiode

When these precautions are taken, it is hoped that there will be no need for additional signal filtering. However, because the severity of the Electromagnetic Interference (EMI) environment is not fully known at this time, the differential receivers are followed by a set of filters. These can be bypassed easily if they, subsequently, are shown as unnecessary.

6.3 COMPARISON WITH HALL TRANSDUCER SIGNALS

Comparing E_d and E_s with the output of the Hall-effect transducer shows that the signals from the Hall transducer and from the lateral-effect photodiode differ only in their amplitude scale factor.

The Hall transducer has an output voltage, after signal conditioning, which is proportional to the scanner mirror position and the excitation voltage. The transducer output is:

$$V_t = CV_e\theta$$

where V_t is the transducer output, V_e is the excitation voltage, θ is the mirror position, and C is the amplitude scale factor.

From the diode sensor equations, it can be seen that the difference amplifier signal is of the same form, where K is proportional to mirror position, I_d corresponds to excitation voltage, and R_t is the amplitude scale factor. The output from the sum amplifier corresponds to the excitation voltage. Therefore, the gain of the transconductance amplifier will be set in such a manner that the two sets of signals are interchangable at the inputs to the cable driver amplifiers. Additionally, provisions are included in the receiver amplifiers to adjust both gain and offset.

By providing signal compatability at this level, the remainder of the scan mirror position circuits, which provide pixel timing pulses and mirror position digitization, remain the same as described in the first quarter report. Furthermore, this signal compatability provides a convenient point to interchange the lateral-effect photodiode and the Hall transducer, in a manner that, if time permits, a comparison may be made between the two methods of mirror position pickoff.

6.4 TEST CONCEPTS

Evaluation of the lateral-effect photodiode as a position tranducer will require both static and dynamic tests for accuracy, linearity, and repeatability.

The static testing, which is the simplest to accomplish, is being performed first. The test fixture for static testing will consist of a light source and the mounted lateral-effect diode (Figure 6-3). In addition, a control arm will be attached to the mirror drive shaft and to a micrometer drive. The arm will transfer the micrometer drive to the mirror shaft, allowing precise positioning of the mirror. The diode will be coupled into a breadborad of the transconductance amplifiers and the sum and difference amplifiers. The output of the amplifiers can then be measured. Next, the static test can be used to determine the null offset, scale factor, accuracy and linearity of the overall transducer system.

The first dynamic tests will establish the dynamic response of the diode and its associated electronics. The light source to be used is a Light-Emitting Diode (LED) which can be amplitude-modulated with essentially flat response up to approximately 500 kHz, which is considerably greater than any frequency of interest. Using the static test fixture just described and a pulsed drive for the light source, the transient response of the diode and associated electronics will be measured at various mirror displacement angles. The delay, rise and fall times, overshoot and ring, and droop of the output signals can then be used to predict the dynamic behavior of the transducer system.

Note that both the static testing and the first steps in dynamic testing can be accomplished without the need for an operating scan mirror assembly and its associated drive electronics. The final dynamic tests will require an operating scan mirror. A single-line target, with known line width, will be directed through one side of the scan mirror to a high-resolution camera. The other side of the scan mirror will direct the light source to the lateral-effect diode (Figure 6-3). The diode electronics will then be coupled to the remainder of the scan mirror position quantizer circuits to produce temporal pixel pulses.

Linearity of the overall system can then be determined by comparing the number of pixel pulses occurring during the time the video pulse is produced by the target line on the camera as it is moved across the entire field of view. Overall accuracy can be determined by comparing the time of occurrence of selected digitized mirror positions to the leading and trailing edges of the video pulses from the camera.

6.5 CURRENT STATUS

A breadboard has been constructed of all diode electronics, including the transconductance amplifiers, the sum and difference amplifiers, the cable driver and receiver amplifiers, and the filter circuits. At present, it is being debugged and evaluated. The evaluation testing will include circuit transient response tests and noise immunity tests, as well as overall circuit performance.

A scan mirror mechanical assembly has been obtained, and the light source assembly has been manufactured. Necessary mounting details, cover plates, and the micrometer drive and control arm have been procurred or manufactured. These are being assembled so that the static testing and first dynamic testing can be completed as soon as the evaluation of the breadboard circuits has been finished.

Final dynamic testing will be scheduled as soon as an operating scan mirror and its associated drive electronics are available.

SECTION 7
SYSTEM MEMORIES

7.1 SCAN CONVERTER

The scan converter memory accepts data from the enhancement circuitry in the Forward-Looking Infrared (FLIR) vertical scan format, stores it in memory, and outputs it to Digital-to-Analog (D/A) converters in normal video raster scan pattern. It also accepts symbology information from the classification processor and outputs that information, at its proper position in parallel with the raster scan, and so that the symbol is placed where required on the video display. A block diagram of the scan converter memory is presented in Figure 7-1.

7.1.1 Input Control Logic

The input control logic receives a clock from the enhancement logic which controls the input of data into the system. There is also a direction signal that indicates whether the data being presented is from the forward or reverse scan of the FLIR. On the basis of this information, the input control logic generates memory control signals and memory addresses to govern the storage of incoming information in the memory.

7.1.2 Refresh Logic

The refresh logic generates memory control pulses that refresh the dynamic memories during retrace times so that information is not lost.

7.1.3 Address Selection

Memory addresses are generated in the input control logic, the output shift register control, and the refresh logic. In addition, both row address and column address must be placed on the memory address lines. The address selection responds to

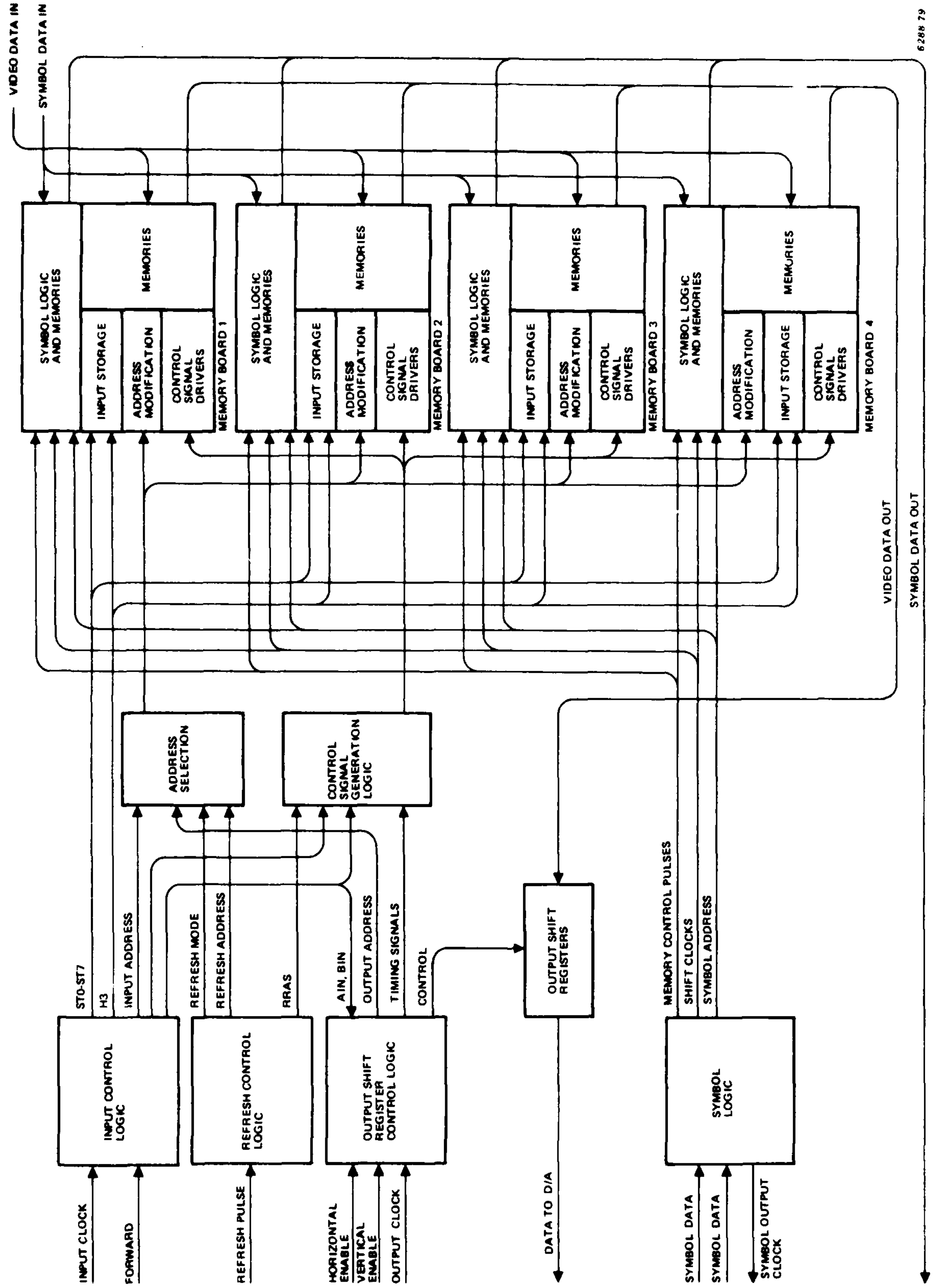

Figure 7-1. Scan Converter Memory Block Diagram

timing signals from the input control logic, the refresh logic and the output shift register control and switches the proper information onto the memory address lines in order to insure orderly storage and retrieval of data in the memory.

7.1.4 Address Modification

In order to achieve the video speed required to output data, it is necessary to interleave eight memory groups in parallel on each output channel. If data were recorded in all groups in identical memory locations, each block of eight output words would end up in the same memory, and the parallel redundancy would be of no value. Therefore, the memory addresses are altered by increments of one for each member of the group of eight. This allows a block of eight output words to be recovered in parallel from the eight memory groups.

7.1.5 Input Storage

Because of the output video speed requirements, it is necessary to assemble a block of four words and store them simultaneously, in parallel, in four (out of eight) successive memory groups. The input storage contains the logic to control this assembly.

7.1.6 Control Signal Drivers

This circuitry merely amplifies the memory timing signals in order to drive the large number of memory circuits in the memory assembly.

7.1.7 Memories

The memories used are 16K bit, dynamic Metal-Oxide Semiconductor (MOS) memory devices.

7.1.8 Output Shift Register Control

The output shift-register control serves two purposes. Because the address modification skews the data by successive increments of address, output data comes out in blocks of eight that have been shifted cyclically (Module 8). The shift registers are used to rotate the blocks so that the first word required is properly placed in the first position in the block. The eight words are then presented to the output interface, in sequence, by shifting registers in time with the output clock from the system controllers. The output shift-register control logic generates the control signals to sequence these events properly.

7.1.9 Output Shift Registers

The output shift registers effect the output sequencing under the control of the signals from the output shift-register control.

7.1.10 Symbol Logic and Memories

Symbology is generated in the ATC by an overlay of two memory planes. The logic to control the memory is divided between the control board and the memory boards. That which is common to all channels is placed on the control board, and that which can be divided into particular channels is placed on the memory board that corresponds to the symbol position. Symbol data is received by the memory from the system controller during vertical retrace time. The symbol data consists of a two-bit word and position information to locate the symbology on the display. The symbol logic converts this position information into row and column address for the symbol memories and generates strobe signals to enter the two bits of data into the memories. Then, during active time, the symbol data is output in parallel with the video data stored in the scan converter memories.

7.2 FRAME MEMORY

Several minor changes have been made to the frame memory since the first quarter report, but only one of them significantly affects the manner in which it operates.

The interface with the circuits has been revised and redesigned to present data to the detector in a steady stream rather than through random access. This stream is controlled by a clock from the detector circuits. The format of the data is a non-interlaced vertical raster scan that starts in the top left corner of the frame and scans to the bottom right. The detector accepts data until it determines that there is an area of interest. It then stops its clock and notifies the silhouetter. Data is output to the silhouetter in random access format until the required information is transferred. Then the transfer of information to the detector is resumed where it was interrupted.

SECTION 8
AUTOMATIC TARGET CUER MODEL 1 CONFIGURATION

The Automatic Target Cuer (ATC) Model 1 configuration consists of three principal hardware units, the ATC main frame, the Forward-Looking Infrared (FLIR) digitizer, which contains the electronic multiplexer, and the scan mirror position sensor. This section describes the mechanical configuration of each unit and shows how they are connected to function as a system.

8.1 ATC MAIN FRAME

The ATC main frame houses most of the electronics within the ATC system. The unit is 21 in. tall by 10 in. deep and fits in a standard 19-in. rack. This rack-mounted feature will facilitate the laboratory development of the ATC. A perspective view of the ATC main frame is shown in Figure 8-1. The ATC layout, showing the distribution of circuit cards for the various functions of the ATC, is presented in Figure 8-2.

The circuit cards used in the ATC main frame are wire-wrapped and come in two different sizes, 10 1/2 in. wide and 5 1/4 in. wide. Both types are 8 1/2 in. high. A budget of circuit cards for each of the ATC functions is given in Table 8-1.

The computers used in the ATC main frame are DEC LSI-11/2's. A backplane containing 8 card slots is provided for each computer. The specific configuration of each computer will depend on the state of development of the algorithms involved. For example, during initial programming the silhouetting computer will contain the Central Processing Unit (CPU), 32 K words of Random Access Memory (RAM), a RS-232 terminal interface, necessary system interfaces, and a floppy disk controller. However, during later stages of development, the terminal interface and the floppy disk will be removed while some of the RAM will be replaced with a Read Only Memory (ROM).

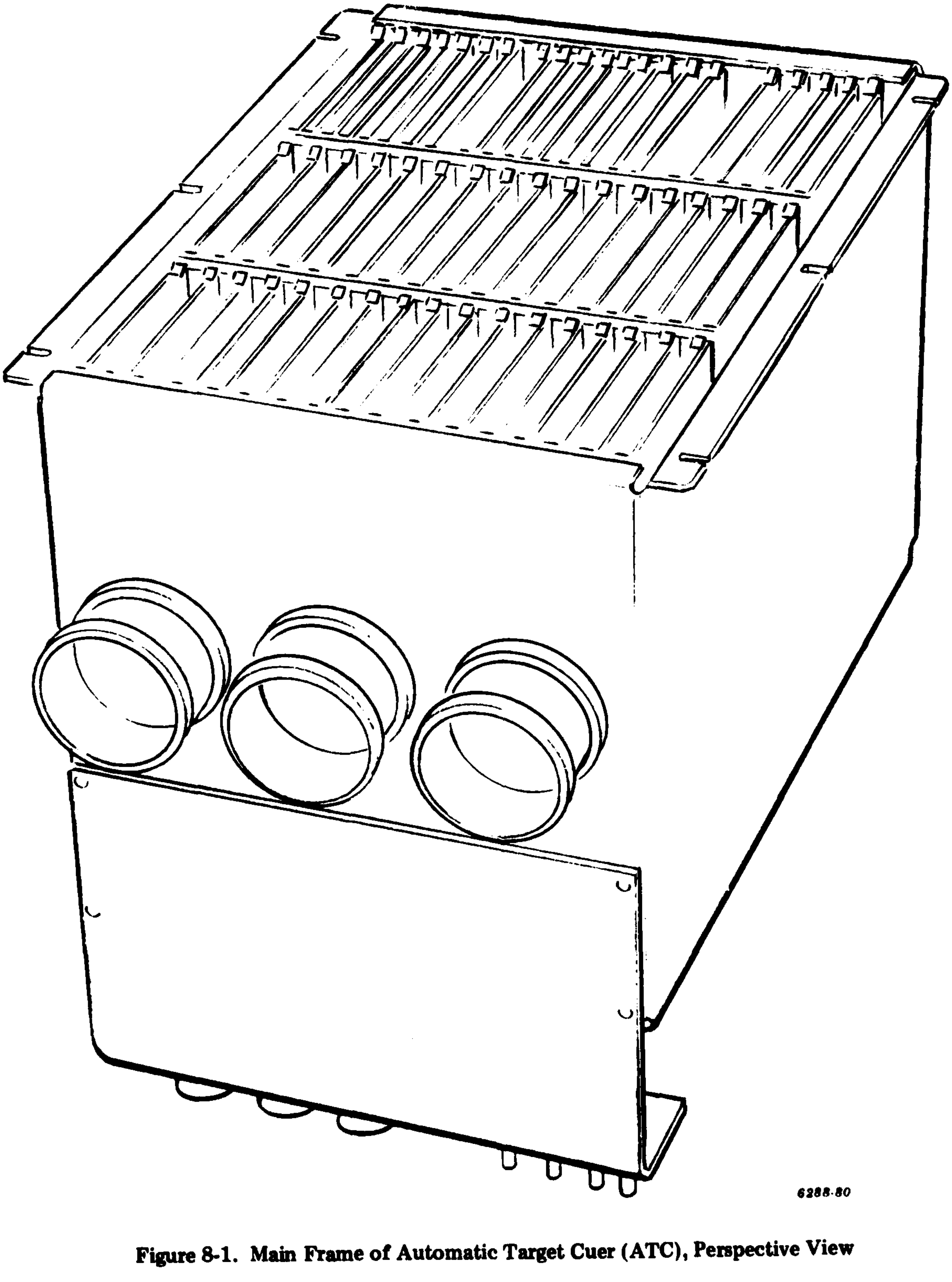

Figure 8-1. Main Frame of Automatic Target Cuer (ATC), Perspective View

Table 8-1. ATC Main Frame Circuit Card Budget

Function	Number of Cards	Size
Scan converter	5	10 1/2 in.
Enhancement	5	10 1/2 in.
Frame store	3	10 1/2 in.
Detector	3	10 1/2 in.
Sync Generator	1	5 1/4 in.
Digital-to-Analog converter	1	5 1/4 in.
Spare	1	10 1/2 in.
Spare	1	5 1/4 in.

8.2 FLIR DIGITIZER

The circuit cards that comprise the Model 1 FLIR digitizer are housed in their own assembly. The dimensions of the FLIR digitizer unit are 38 in. by 12 1/2 in. by 5 1/2 in. A perspective view of the FLIR digitizer is shown in Figure 8-3.

The FLIR digitizer contains slots for 38 circuit cards that are utilized according to the layout given in Figure 8-4. The circuit cards are arranged to provide for the maximum separation of analog and digital signals. For example, the interface amplifiers for each channel are located at the ends of the FLIR digitizer while the Analog-to-Digital (A/D) conversion takes place more toward the center area.

The circuit cards in the FLIR digitizer are all 3 1/2 in. by 8 in. and are budgeted as given in Table 8-2. The power and ground planes are printed on each of the cards. However, the interconnecting wiring is implemented using the multiwire technique as presented in MIL-M-83436 (USAF). This method of circuit implementation uses wires embedded in a resin-based material rather than etched metal to provide electrical interconnection on the card. Multiwire is used because it is more cost effective than multiple layer printed circuit cards.

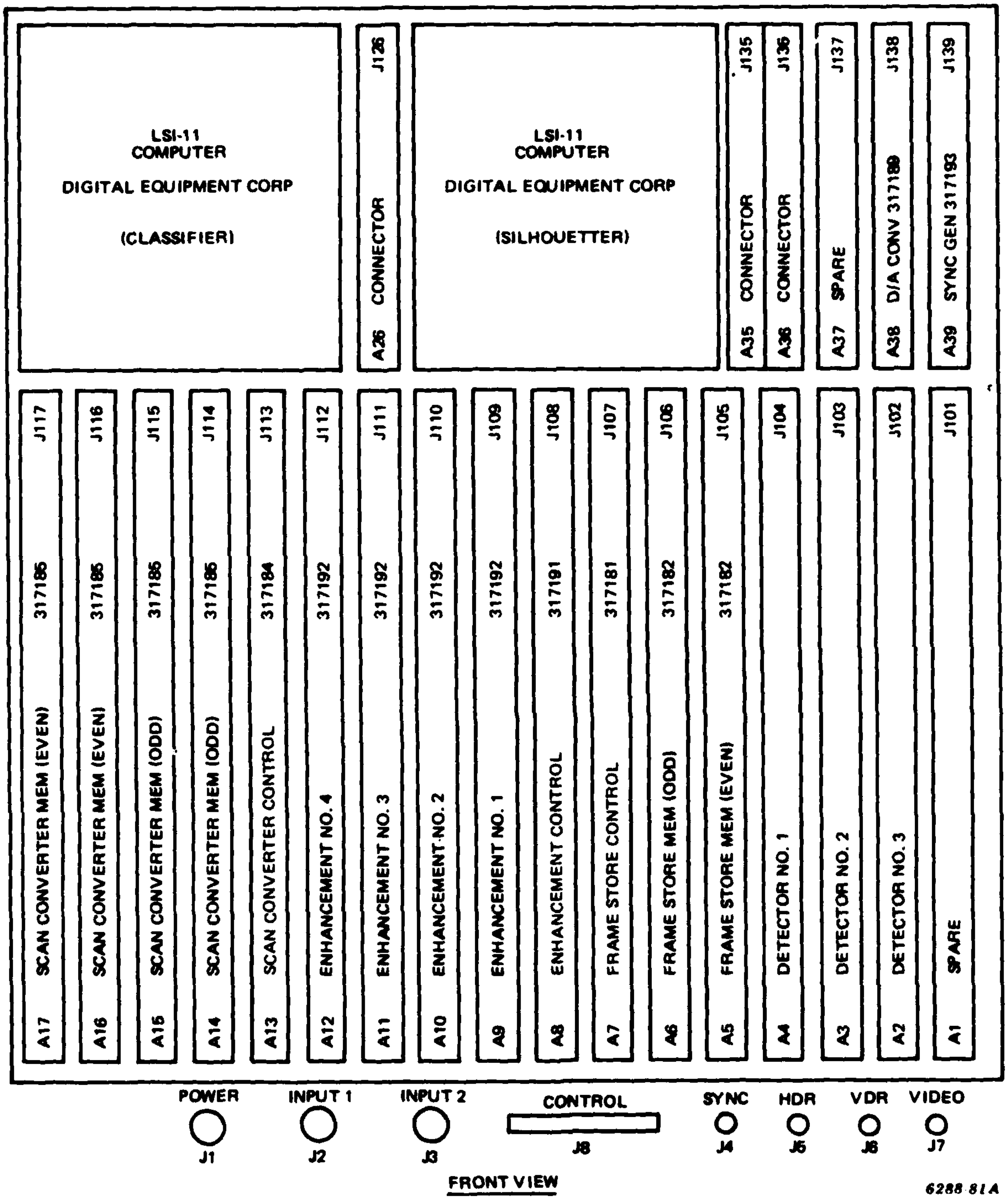

Figure 8-2. Layout for the Main Frame of the ATC

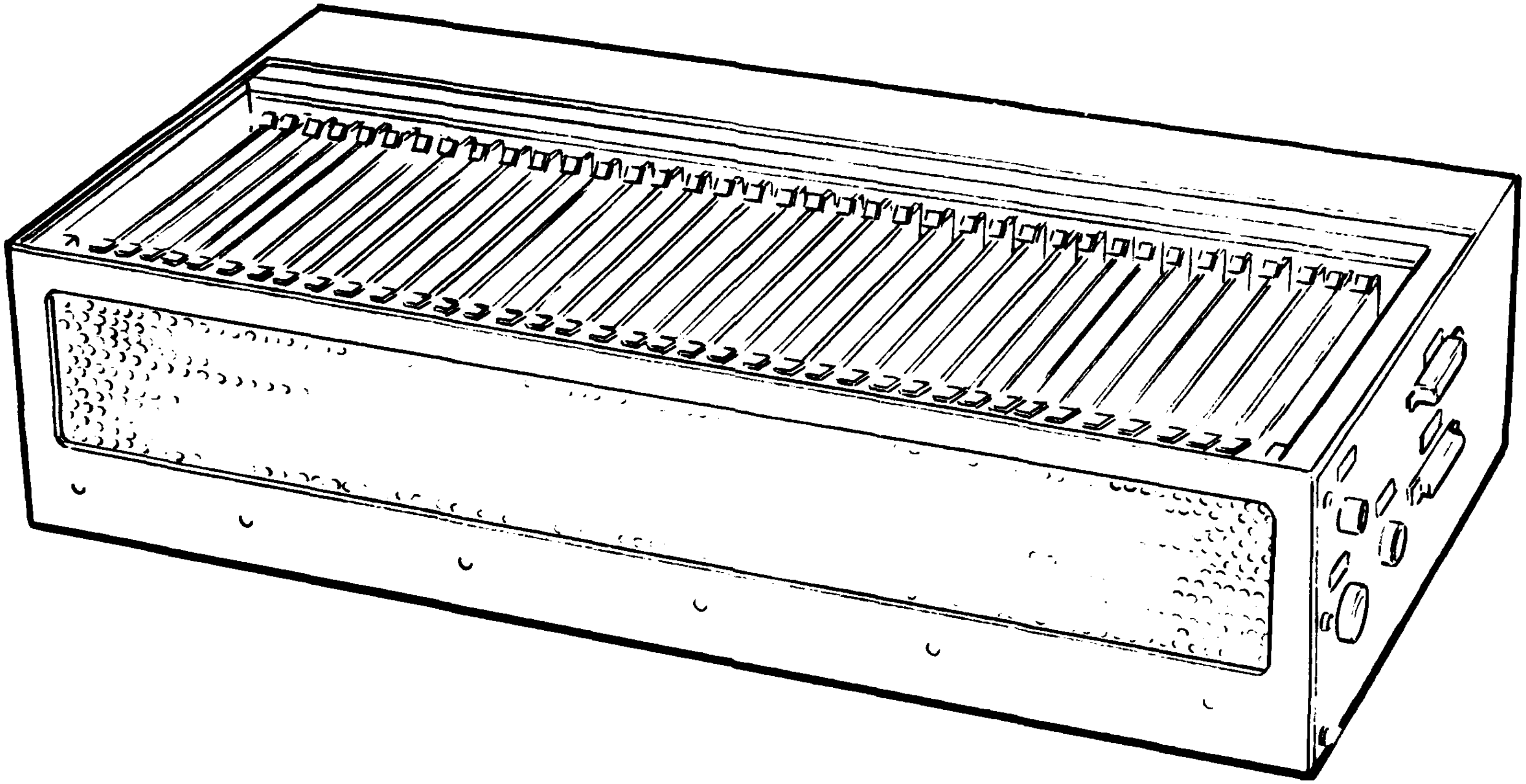

Figure 8-3. FLIR Digitizer, Perspective View

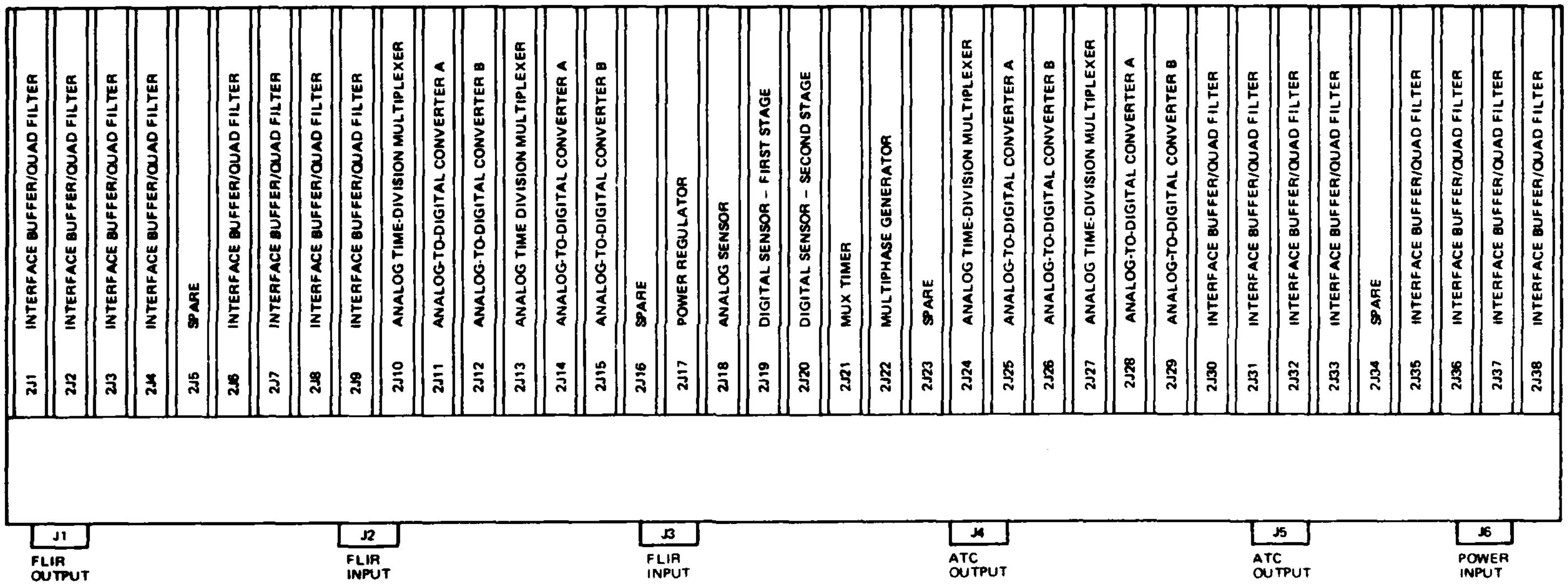

Figure 8-4. Layout for the FLIR Digitizer

Table 8-2. FLIR Digitizer Circuit Card Budget

Function	Number of Cards
Interface buffer/filters	16
Multiplexer	4
A/D converter	8
Multiplexer controller MUX timer	1
Multiphase Generator	1
Power Regulator	1
Mirror Position Sensor Analog	1
Mirror Position Sensor Digital	2
Spare	4

8.3 SCAN MIRROR POSITION SENSOR

The scan mirror position sensor consists of two separate units that are both mounted on the FLIR mechanical scanner common module. The first unit contains an Infrared (IR) Light-Emitting Diode (LED) that shines IR light toward the scan mirror. The second unit has the optics necessary to focus the reflected image of the IR LED onto a lateral-effect photodiode. The photodiode and its associated electronics are also housed in the second unit. Figure 8-5 shows photographs of the IR LED light source and photo detector (minus electronics) both separately and mounted on the FLIR scanner module. These units will be mounted in the Light Observation Helicopter Target Acquisition/Designation System (LOHTADS) FLIR, as shown in Figure 8-5.

8.4 INTERCONNECTIONS

The interconnecting cabling for the ATC Model 1 system is diagrammed in Figure 8-6. The LOHTADS FLIR has three signal cables connecting it to the FLIR digitizer. Two of the cables contain the IR image information obtained from the FLIR post amps (60 channels/cable). The third cable has the signals necessary to represent the FLIR scan mirror position.

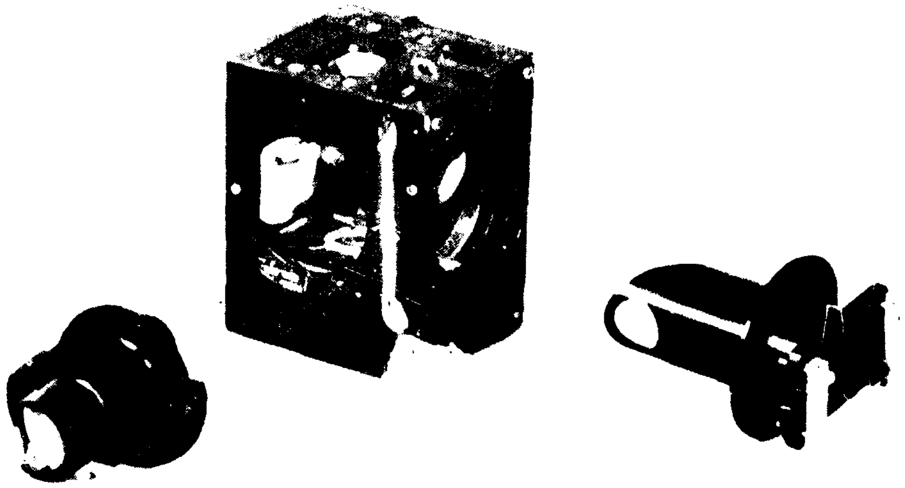

(a) DISASSEMBLED

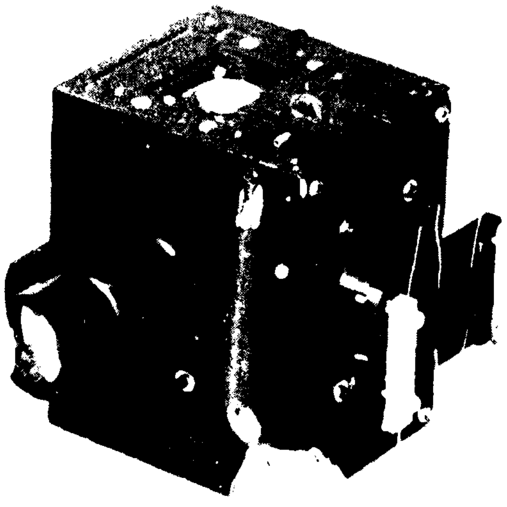

(b) ASSEMBLED

6288-122

Figure 8-5. Infrared Light Source and Detector

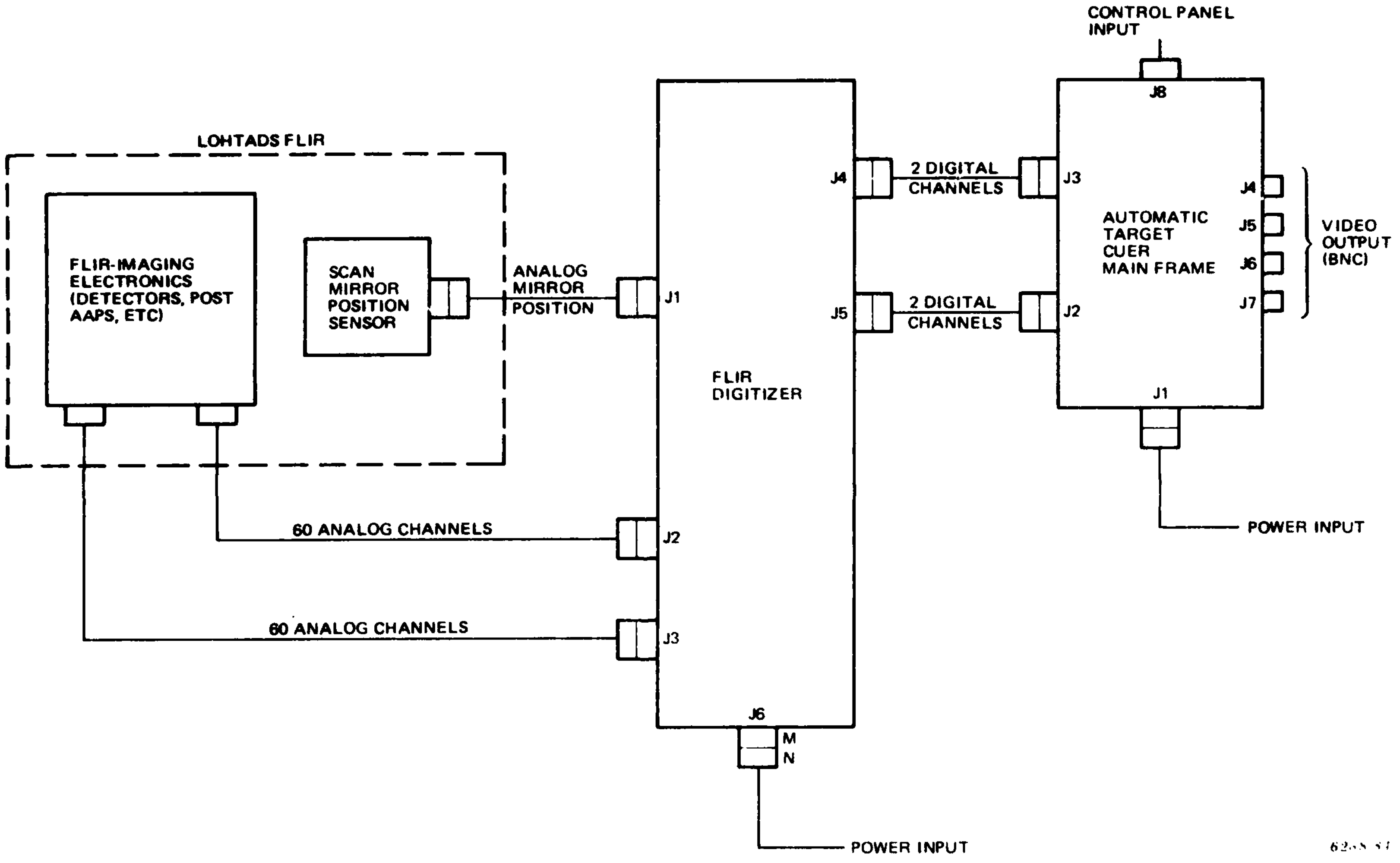

Figure 8-6. Interconnecting Cabling , Model 1 ATC System

The FLIR digitizer routes the multiplexed digital FLIR image to the ATC main frame via two cables. Each cable carries two separate multiplexed digital channels. The ATC main frame receives the digitized imagery and generates RS-343 video with appropriate target cues. The cued video is available at several video coaxial connectors on the ATC main frame.

SECTION 9
STATUS AND PLANS FOR NEXT QUARTER

The status and plans of each aspect of the Automatic Target Cuer (ATC) program are summarized in this section.

9.1 IMAGE ENHANCEMENT

The design of the image enhancement circuitry has been completed. The circuit cards that perform the image enhancement have been wire-wrapped and will be checked out during the next quarter.

9.2 TARGET SILHOUETTER

The algorithms of the silhouetting system have been improved and tested on a larger data base. Next quarter's effort will include the integration of region labelling and any necessary refinements to the silhouetting system. The design of the hardware to perform silhouetting will begin during the next quarter.

9.3 TARGET DETECTION

The target detection effort is divided into two parts, target filtering and target location. The target location algorithms have been defined, and hardware design will begin next quarter. The algorithms for target filtering are 75 per cent complete and still must undergo test on a large data base. Testing and completion of the filtering algorithms will be accomplished during the next quarter. This effort will be aided by the data base encoding efforts described in paragraph 9.8.

9.4 TARGET CLASSIFICATION

The feature set that performed optimally on a 58-target test set was shown to be the University of Maryland feature set. This feature set will be used in the ATC Model 1 system. During the next quarter methods of assigning points in feature space to target classes will be examined.

9.5 FORWARD-LOOKING INFRARED (FLIR) DIGITIZER

The breadboarding of a single multiplex group has been completed. Also, the design of the multiplexer is complete, and printed circuit layout is underway. During the next quarter the printed circuit cards will be completed, and the FLIR digitizer will begin checkout.

The scan mirror position sensor design has been completed. The design uses a large-area photodiode as the sensing element. The sensor itself has been constructed, and its attendant electronics are undergoing breadboard and test. The sensor electronics will be completed in the third quarter.

The FLIR digitizer will be integrated and tested during the upcoming quarter in order to be ready for the FLIR Government-Furnished Equipment (GFE) on 17 March.

9.6 SYSTEM MEMORIES

The designs of the frame memory and scan converter memory are complete. The circuit cards have been wire-wrapped and will be tested next quarter.

9.7 INSTRUMENTATION SYSTEM

The instrumentation system consisting of the CAI LSI-2 computer and its interface to the frame memory is 80 per cent complete. It will be completed during the next quarter and used for checkout of the rest of the ATC hardware.

9.8 DATA BASE

Because of laboratory simulation system hardware problems, the target subframe data base has not been expanded this quarter as planned. The problems have been corrected, and work toward expanding the target data base will resume next quarter. The planned expansion includes a transfer of the image data sets from tape to disk media. Also, the ground truth of each image will be encoded in a computer readable format at the front of each image.

-8

DTIC